

Pull-in and snap-through instabilities in transient deformations of microelectromechanical systems

K Das and R C Batra

Department of Engineering Science and Mechanics, M/C 0219, Virginia Polytechnic Institute and State University, Blacksburg, VA 24061, USA

E-mail: kdas@vt.edu and rbatra@vt.edu

Received 9 October 2008, in final form 25 November 2008

Published 5 February 2009

Online at stacks.iop.org/JMM/19/035008

Abstract

We analyze transient finite electroelastodynamic deformations of a perfect electrically conducting undamped clamped–clamped beam, a clamped–clamped parabolic arch and a clamped–clamped bell-shaped arch suspended over a flat rigid semi-infinite perfect conductor. The pull-in instability in a beam and the pull-in and the snap-through instabilities in the two arches due to time-dependent potential difference between the two electrodes have been studied. The potential difference is applied either suddenly or is increased linearly in time. Since the time scale of the transient electric forces is very small as compared to that of the mechanical forces, inertia effects only in the mechanical deformations are considered. Effects of both material and geometric nonlinearities are incorporated in the problem formulation and solution; however, damping due to the interaction of the structure with the surrounding medium is neglected. The coupled nonlinear partial differential equations for mechanical deformations are solved numerically by the finite element method and those for the electrical problem by the boundary element method. The Coulomb pressure due to the potential difference between the two electrodes is a nonlinear function of the *a priori* unknown distance between them. The potential difference that induces either the pull-in instability in a beam or the snap-through followed by the pull-in instabilities in an arch has been computed. Wherever possible these results are compared with those available in the literature. With a decrease in the rate of the applied potential difference, the pull-in and the snap-through parameters approach those for a static problem. Also, for large rates of increase in the potential difference between the two electrodes, the snap-through instability in an arch is suppressed and only the pull-in instability occurs.

(Some figures in this article are in colour only in the electronic version)

1. Introduction

Microelectromechanical systems (MEMS) having components of dimensions in the range of a few to a hundred micrometers are used as radio frequency (RF) switches, varactors and inductors [1], accelerometers [2], pressure sensors, controllers for micro-mirrors [3], micro-pumps [4] and bio-MEMS [5]. A number of different actuation properties, such as piezoresistive, piezoelectric, electrostatic, electromagnetic, thermal and optical, have been exploited in MEMS. Of these, the electric actuation is widely

used because of the low power consumption and potential for integration in a standard integrated circuit environment. An electrically actuated MEMS consists of a deformable electrode made of a conductive material suspended above a rigid conductive electrode with a dielectric medium, generally air, between them. An electric potential difference applied between the two electrodes induces the Coulomb pressure on the electrodes which deflect the deformable electrode toward the rigid one. The elastic restoring force induced in the deformed electrode restricts its motion. Electric charges redistribute on the deformable electrode's surface and the gap

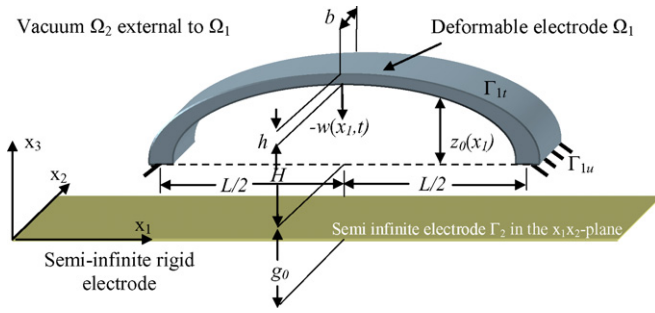


Figure 1. Schematic sketch of the problem studied.

between it and the rigid electrode decreases, which in turn increases the Coulomb force and deforms the deformable electrode more until the elastic restoring force is balanced by the Coulomb force.

1.1. The pull-in instability in MEMS

For electrically actuated MEMS, the applied electric potential has an upper limit, beyond which the corresponding Coulomb force is not balanced by the elastic restoring force, resulting in sudden collapse of the deformable electrode on the rigid one. This phenomenon, called the pull-in instability, was observed experimentally by Taylor [6] and Nathanson *et al* [7]. The corresponding values of the potential difference and the peak displacement of the deformable electrode are called the pull-in voltage and the pull-in displacement, respectively; collectively the two are called pull-in parameters.

Accurate estimates of pull-in parameters are crucial for designing electrically actuated MEMS. In switching applications [8], the pull-in instability is necessary for the switch to operate. However, for micro-mirrors [9] and micro-resonators [10], the pull-in instability restricts the range of operational displacement of the device.

1.2. The snap-through instability in an arch-shaped MEMS

In an arch-shaped deformable electrode (e.g., see figure 1), in addition to the pull-in instability, the snap-through instability can occur under the Coulomb pressure; these two instabilities have been studied in [11, 12] with a one-degree-of-freedom system. Figure 2 shows a bifurcation diagram between the peak displacement w of an arch-shaped MEM electrode and the electric potential difference parameter β defined as $\epsilon_0 b L^4 V^2 / 2 E I g_0^3$. Here ϵ_0 is the vacuum permittivity, b is the width, L is the length, g_0 is the initial gap, V is the electric potential difference between the two electrodes, E is Young's modulus and I is the second moment of the cross-section of the deformable electrode about the neutral axis. The bifurcation diagram has two stable branches AC and DF. Initially, with the increase in β , w increases gradually from point A to point C, the arch maintains its initial curved shape and the resultant elastic restoring force balances the Coulomb force. At point C, the deflection increases suddenly, and the arch is inverted to a new equilibrium position corresponding to

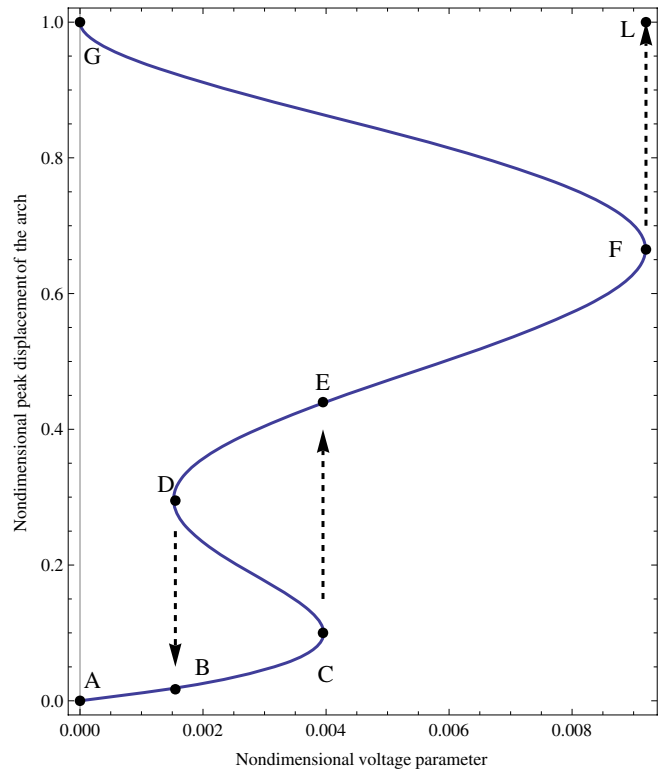


Figure 2. Bifurcation diagram for the snap-through and the pull-in instabilities of arch-shaped MEMS (from [12]).

point E. This sudden jump in the deflection is called the snap-through instability and the corresponding voltage the snap-through voltage. From point E to point F, the elastic restoring force induced in the arch again balances the Coulomb force. However, just after point F, the deformable electrode collapses on to the rigid one and the pull-in occurs. The portions CD and FG of the curve are unstable. During the loading process, the arch follows the path ACEFL, and it follows the path FDDBA during unloading.

Advantages of the snap-through instability have been exploited in actuators [13–16], microvalves [17] and transducers [18]. The snap-through instability of an arch-shaped MEMS under slowly applied electric loads has been observed experimentally and studied through reduced-order models in [11, 12, 19, 20].

The snap-through instability of an arch is not guaranteed. Various conditions such as the arch rise H (see figure 1) for different arches (parabolic, circular or sinusoidal), arch thickness h , type of loads (step or ramp) and the gap g_0 between the electrodes determine whether the snap-through will occur. Pippard [21] and Patricio *et al* [22] have presented a phase diagram between the arch length and the initial arch angle at the clamped end, showing conditions for which the snap-through can occur due to a quasistatic mechanical point load, which is not dependent on arch deflection; they studied different arch configurations either experimentally or numerically and joined the points to get the phase plot. Zhang *et al* [19] and Krylov *et al* [20] have studied static problems involving the snap-through and the pull-in instabilities in circular and bell-shaped arches, respectively. Krylov *et al* [12] have presented a phase

diagram between H and h showing conditions for which the snap-through can occur in static deflections of a bell-shaped MEMS. Zhang *et al* [19] explained that the snap-through and the pull-in instabilities can only be distinguished by the physical criterion of whether or not the collision between the deformable and the rigid electrodes occurs. Depending on the arch shape and the load type, the following three scenarios arise: either only the pull-in instability occurs, or the arch undergoes the snap-through and then the pull-in instability, or the snap-through and the pull-in occur simultaneously. In each case, the pull-in instability occurs.

1.3. The dynamic pull-in and snap-through instabilities

In dynamic loading, transient effects may trigger either the snap-through or the pull-in instability first. The pull-in instability in a MEMS under a transient electric load has been studied in [23–28], and the snap-through of arches and shells during their transient deformations under mechanical loads has been reported in [29, 30]. The snap-through of laminated composite spherical caps during their transient deformations under mechanical loads has been studied in [31, 32]. Identifying the pull-in instability is easy because of the physical phenomenon of the deformable electrode touching the rigid one. The ‘dynamic snap-through’ generally means a large increase in response, resulting from a small increase in a load parameter [29]. Simitses [33] has proposed that for static deformations under a distributed mechanical load, the arch rise parameter, $e_{\text{arch}} = 2\sqrt{3}H/h$, must be greater than 5.0 for the snap-through instability to occur in a shallow arch defined as one for which $(dz_0(x_1)/dx_1)^2 < 0.05$, where $z_0(x_1)$ is the shape of the bottom surface of the arch; see figure 1. However, e_{arch} must be greater than 5.86 and 9.73, respectively, for a step load described by a Heaviside function and an impulsive load given by a Dirac delta function. Thus, conditions for the dynamic snap-through to occur depend not only on geometric parameters of the arch, but also on the type of loads. As far as we can determine, the combined snap-through and pull-in instabilities in transient deformations of arch-shaped MEMS have not been analyzed.

1.4. Modeling of electrically actuated MEMS

The modeling of electrically actuated MEMS has been reviewed in [34]. In most cases, the Coulomb pressure on the electrodes has been computed by using the parallel plate approximation (PPA) which assumes that the two electrodes are locally parallel to each other. In order to alleviate the computational difficulty of a 3D analysis, a number of reduced-order models approximating the deformable electrode as a beam [35–40] have been developed. If the aspect ratio of the deformable electrode is large, approximation of the electrode as a plate is more appropriate [41–51]. Many MEMS devices, such as micro-pumps made of thin glassy polymers, and grating light valves consisted of stretched ribbons, can be approximated as membranes, e.g. see [25, 52–54].

Reduced-order models estimate global quantities, such as the natural frequency or the deflected shape of the deformable electrode, with reasonable accuracy; they cannot predict

accurately local quantities such as the stress and the strain in a MEM electrode of arbitrary geometry. Therefore, for analysis, design, optimization and product development of MEMS devices, continuum mechanics based simulations are necessary.

Nishiguchi and Sasaki [55] have presented a large deformation theory for solids subjected to electromagnetic loads but did not solve any engineering problem. Gilbert *et al* [56] developed the software CoSolve-EM to solve 3D quasi-static electro-mechanical problems; it couples the FE code ABAQUS and the BE code FASTCAP: the former for analyzing mechanical problems and the latter for electrical problems. They did not solve a transient problem. The commercial software COMSOL can be used to study MEMS problems using the FEM with the Eulerian description of motion for the electric field in the medium surrounding the electrodes and the Lagrangian description of motion for deformations of the electrode. It needs frequent re-meshing of the region exterior to the MEM electrodes for analyzing both static and transient problems, which requires considerable computational resources. Shapoorabadi and Andrew [57] have compared three different methods available in the commercial FE software ANSYS, namely (1) ESSOLV: a sequentially coupled electrostatic and structural field tool, (2) TRANS126: a directly coupled electrostatic and structural field tool employing 1D transducer element and (3) ROM144: a directly coupled electrostatic and structural reduced-order model. They studied static infinitesimal deformations of a torsional and a flexural-torsional micromirror and concluded that predictions from the ROM144 and the ESSOLV compare well with analytical and experimental results. However, for problems involving large deformations, the TRANS126 should be used instead of the ROM144 and the ESSOLV. They too did not consider transient problems.

De and Aluru [58] used the coupled finite cloud and the boundary cloud methods to convert partial differential equations (PDEs) describing the balance of linear momentum and the charge conservation to ODEs in time and solved them using Newton’s and the relaxation schemes. They employed the Lagrangian description of motion, computed exactly the Jacobian matrix in Newton’s method, modeled the MEM electrodes as 2D bodies and neglected effects of fringing fields and material nonlinearities.

From the literature review given above, it can be concluded that transient deformations of arch-shaped MEMS considering both material and geometric nonlinearities have not been studied. Here, we describe a mathematical model for studying 3D problems and develop the needed software to analyze the mechanical problem by the FEM and the electrical problem by the BEM. The two are coupled with information exchanged between them after every time step. After validating the mathematical model, we study the pull-in and the snap-through instabilities in arch-shaped MEMS under time-dependent potential difference.

The rest of the paper is organized as follows. Section 2 presents governing equations for MEMS using continuum balance laws and Maxwell’s equations, and the numerical technique to solve the system of governing equations. In

section 3, results for flat and arch-shaped MEMS are described and discussed. We summarize conclusions from the present work in section 4.

2. Mathematical model

2.1. Balance laws for MEMS

A schematic sketch of the problem studied is shown in figure 1 that also exhibits the rectangular Cartesian coordinate axes used to describe deformations of the bodies. The deformable electrode is modeled as a perfectly conductive solid body undergoing finite deformations and the rigid electrode as a semi-infinite plate in the x_1x_2 plane. Let $\Omega_1 \subset \mathfrak{R}^3$ and $\Gamma_2 \subset \mathfrak{R}^2$ be regions occupied by the deformable electrode and the rigid semi-infinite electrode, respectively; $\Omega_2 \subset \mathfrak{R}^3$ is the semi-infinite region surrounding Ω_1 and situated above the electrode Γ_2 , and is vacuum. Γ_1 is the boundary of Ω_1 with disjoint parts Γ_{1u} and Γ_{1r} . The kinematic and the traction boundary conditions are prescribed, respectively, on Γ_{1u} and Γ_{1r} . The reference configurations Ω_1 and Ω_2 are deformed into the current configurations $\omega_1 \subset \mathfrak{R}^3$ and $\omega_2 \subset \mathfrak{R}^3$, respectively; γ_1 is the boundary of ω_1 , and γ_2 is the image of Γ_2 in the current configuration. We note that $\Gamma_2 = \gamma_2$ since the bottom electrode is rigid. We denote position vectors of a point with X_i and x_i ($i = 1, 2, 3$) in the reference and in the current configurations, respectively.

The electric field vanishes in a perfect conductor. Thus, no net charge is present inside the body. The motion of the deformable electrode Ω_1 is governed by the balance of mass, the balance of linear momentum and the balance of moment of momentum, given respectively by equations (1), (2) and (3) in the referential description:

$$\rho J = \rho_0 \quad (1)$$

$$\rho_0 \dot{v}_i = \frac{\partial \hat{T}_{ji}}{\partial X_j} + \rho_0 f_i \quad \text{in } \Omega_1 \quad (2)$$

$$\hat{T}_{ik} F_{kj} = \hat{T}_{jk} F_{ki} \quad \text{in } \Omega_1. \quad (3)$$

The coupling between the mechanical and the electrical effects is through the Coulomb pressure which acts as tractions on the surface Γ_{1r} of the electrode. Deformations of Γ_1 influence the electric field in Ω_2 since Γ_1 is also a boundary surface of Ω_2 . In equations (1)–(3), ρ_0 and ρ are mass densities in the reference and the current configurations, respectively; J is the determinant of the deformation gradient $F_{ij} = \frac{\partial x_i}{\partial X_j}$, v_i is the velocity field defined as $v_i = \dot{x}_i$, a superimposed dot denotes the material time derivative, \hat{T}_{ij} is the first Piola–Kirchhoff stress tensor, f_i is the body force per unit mass and a repeated index implies summation over the range of the index. The first Piola–Kirchhoff stress tensor is related to the Cauchy stress tensor T_{pj} by

$$\hat{T}_{ij} = J \frac{\partial X_i}{\partial x_p} T_{pj}. \quad (4)$$

2.2. Electrostatic approximations

The electric and the magnetic fields in Ω_2 are governed by Maxwell’s equations [59]. Since the characteristic time scale

of mechanical deformations is much larger than that of inertia effects in Maxwell’s equations, therefore we neglect the time dependence of electric and magnetic fields there by eliminating coupling between magnetic and electric fields. Henceforth, we consider electric fields only, and assume that a scalar potential $\phi(x_i, t)$ exists. The electric field E_i^{elec} is given by

$$E_i^{\text{elec}} = -\frac{\partial \phi}{\partial x_i}. \quad (5)$$

2.3. Constitutive relations

Even though the problem formulation and the analysis technique are applicable to a general material, for simplicity we presume that the deformable electrode is composed of a neo-Hookean material for which

$$T_{ij} = \lambda E_{ll} \delta_{ij} + 2\mu E_{ij} \quad (6)$$

where λ and μ are elastic constants for the material of the body Ω_1 and E_{ij} is the Almansi–Hamel strain tensor defined as

$$E_{ij} = \frac{1}{2}(\delta_{ij} - (F^{-1})_{li}(F^{-1})_{lj}). \quad (7)$$

Note that equation (7) considers all geometric nonlinearities, including the von Karman nonlinearity. With the constitutive assumption (6), the balance of moment of momentum equation (3) is identically satisfied, and only geometric nonlinearities are considered. Material damping due to viscous effects can be incorporated by modifying the constitutive relation (6).

2.4. Simplified governing equations

Assuming that there are no free charges in ω_2 , the electric potential distribution in the current configuration is governed by the Laplace equation

$$\frac{\partial^2 \phi}{\partial x_i \partial x_i} = 0 \quad \text{in } \omega_2. \quad (8)$$

Therefore, equations (2) and (8) constitute governing equations for the MEMS. Substitution for E_{ij} from equation (7) into equation (6) and the result into equation (4) gives the first Piola–Kirchhoff stress tensor in terms of displacement field u_i defined as

$$u_i(X_l, t) = x_i - X_i(X_l, t). \quad (9)$$

Substitution from equations (6) and (9) into equation (4) and the result into equation (2) gives a set of coupled nonlinear PDEs for the determination of the displacement field. Knowing the displacement field, the present mass density can be found from equation (1).

2.5. Initial and boundary conditions

We assume that initially the deformable electrode is at rest and occupies the reference configuration at time $t = 0$. That is

$$u_i(\mathbf{X}, 0) = 0 \quad (10)$$

and

$$v_i(\mathbf{X}, 0) = 0. \quad (11)$$

For equation (8)

$$\phi \text{ is specified as non-zero on } \gamma_1 \quad (12)$$

and

$$\phi = 0 \quad \text{on } \gamma_2. \quad (13)$$

For equation (2), $u_i(X_l, t)$ is specified on Γ_{1u} for all t and

$$\hat{T}_{ji}N_j = T_i^0 \quad \text{on } \Gamma_{1t} \text{ for all } t. \quad (14)$$

Here, N_i is an outward unit normal vector on Γ_{1t} and T_i^0 is the electrostatic traction given by

$$T_i^0 = \frac{(\sigma_{\text{sur}})^2}{2\epsilon_0} J(F^{-1})_{ji}N_j \quad (15)$$

$$\sigma_{\text{sur}} = -\epsilon_0 \frac{\partial \phi}{\partial x_i} n_i. \quad (16)$$

In equations (15) and (16), σ_{sur} is the charge density on the surface of the deformed electrode and n_i is an outward unit normal vector on γ_{1t} . Note that the coupling between equations (2) and (8) is through equations (14)–(16).

2.6. Numerical solution of the initial-boundary-value problem

We seek an approximate solution of the nonlinear coupled initial-boundary-value problem defined by equations (2) and (8)–(16). The FEM is employed to solve the linear momentum equation (2) because previous research [60] has shown that, at least at the present time for transient problems, the FEM is computationally more efficient than a meshless method. To solve Laplace’s equation, the BEM is used because it can easily consider the semi-infinite domain ω_2 . The FEM and the BEM are described in [61, 62].

We take the inner product of both sides of equation (2) with a test function V_i , which vanishes on Γ_{1u} , and integrate both sides of the resulting equation over the domain Ω_1 to obtain

$$\int_{\Omega_1} \left(\frac{\partial \hat{T}_{ji}}{\partial X_j} + \rho_0 f_i \right) V_i \, d\Omega = \int_{\Omega_1} \rho_0 \ddot{u}_i V_i \, d\Omega. \quad (17)$$

Using the chain rule of calculus, the divergence theorem and the natural boundary condition (14), we get

$$\int_{\Omega_1} \rho_0 \ddot{u}_i V_i \, d\Omega = \int_{\Gamma_{1t}} T_i^0 V_i \, d\Gamma - \int_{\Omega_1} \left(\hat{T}_{ji} \frac{\partial V_i}{\partial X_j} - \rho_0 f_i V_i \right) d\Omega. \quad (18)$$

We express the test function and the trial displacement in terms of basis functions $\psi_a(X_l)$, $a = 1, 2, \dots$, as $V_i(X_l) = \bar{V}_{ai}\psi_a(X_l)$, $u_i(X_l, t) = \bar{u}_{bi}(t)\psi_b(X_l)$, $a, b = 1, 2, \dots$, where \bar{u}_{bi} is the value of u_i at node b , and conclude from equation (18) the following:

$$M_{ab}\bar{u}_{bi} = \hat{F}_{ai}, \quad i = 1, 2, 3 \quad (19)$$

where

$$M_{ab} = \int_{\Omega_1} \rho_0 \psi_b \psi_a \, d\Omega \quad (20)$$

and

$$\hat{F}_{ai} = \int_{\Gamma_{1t}} T_i^0 \psi_a \, d\Gamma - \int_{\Omega_1} \left(\hat{T}_{ji} \frac{\partial \psi_a}{\partial X_j} - \rho_0 f_i \psi_a \right) d\Omega. \quad (21)$$

Note that \hat{F}_{ai} depends on \hat{T}_{ij} , which is related to u_i through the constitutive relation (6) and the strain–displacement relation (7), and T_i^0 , which depends on the charge distribution on the surface of the electrode through equations (15) and (16).

Using the identity

$$[M] \frac{d}{dt} \{\bar{u}\} - [M] \{\dot{\bar{u}}\} = \{0\}, \quad (22)$$

equation (22) can be written in the matrix (or the state space) form as

$$\begin{bmatrix} [M] & 0 \\ 0 & -[M] \end{bmatrix} \frac{d}{dt} \begin{Bmatrix} \{\dot{\bar{u}}\} \\ \{\bar{u}\} \end{Bmatrix} + \begin{bmatrix} 0 & 0 \\ [M] & 0 \end{bmatrix} \begin{Bmatrix} \{\dot{\bar{u}}\} \\ \{\bar{u}\} \end{Bmatrix} = \begin{Bmatrix} \{\hat{F}\} \\ \{0\} \end{Bmatrix}. \quad (23)$$

Equation (23) is integrated with respect to time by using the subroutine LSODE (livermore solver for ODEs) [63].

The salient feature of our FE formulation is that no assumption has been made with regard to the constitutive relation, which relates the first Piola–Kirchhoff stress tensor to the displacement gradient and/or the velocity gradient. Therefore, a wide class of materials, such as linear and nonlinear elastic, viscoelastic and viscoplastic, can be considered for the MEM electrode of arbitrary geometry; e.g. see [70, 71] for the analysis of thermoelastoviscoplastic piezoelectric problems.

The solution of equation (8) in ω_2 is [62]

$$\begin{aligned} \phi(\mathbf{x}_0) = & -\frac{4\pi}{\alpha} \int_{\gamma_1} G(\mathbf{x}, \mathbf{x}_0) [n(\mathbf{x}) \cdot \nabla \phi(\mathbf{x})] \, d\Gamma_1(\mathbf{x}) \\ & + \frac{4\pi}{\alpha} \int_{\gamma_1}^{PV} \phi(\mathbf{x}) [n(\mathbf{x}) \cdot \nabla G(\mathbf{x}, \mathbf{x}_0)] \, d\Gamma_1(\mathbf{x}) \end{aligned} \quad (24)$$

where \mathbf{x} and \mathbf{x}_0 are the field point and the source point, respectively, α is the external angle at \mathbf{x}_0 , ∇ is the gradient operator with respect to \mathbf{x} , PV over the integration sign indicates the Cauchy principal value of the integral and $G(\mathbf{x}, \mathbf{x}_0)$ is Green’s function of the first kind.

When analyzing a plane strain problem in the x_1x_3 plane, we set $x_2 = X_2$ and solve the mechanical problem for u_1 and u_3 . For studying a plane stress problem in the x_1x_3 plane, we set $T_{22} = 0$ in equation (6), solve the resulting equation for E_{22} , substitute for E_{22} in equations for T_{11} , T_{33} and T_{13} and solve the mechanical problem for displacements u_1 and u_3 . For both plane stress and plane strain problems, we solve the electrical problem in the x_1x_3 plane and use the following Green’s function:

$$G(\mathbf{x}, \mathbf{x}_0) = -\frac{1}{2\pi} \ln(r_{\text{dis}}) + \frac{1}{2\pi} \ln(r_{\text{dis}}^{\text{Im}}) \quad (25)$$

where $r_{\text{dis}} = |\mathbf{x} - \mathbf{x}_0|$, $r_{\text{dis}}^{\text{Im}} = |\mathbf{x} - \mathbf{x}_0^{\text{Im}}|$ with $\mathbf{x}_0 = (x_1^0, x_3^0)$ and $\mathbf{x}_0^{\text{Im}} = (x_1^0, -x_3^0)$. The first term on the right-hand side of equation (25) is the free-space Green’s function for the source point \mathbf{x}_0 , and the second term is Green’s function for the source point \mathbf{x}_0^{Im} which is the image of \mathbf{x}_0 with respect to the plane $x_3 = 0$. Therefore, $G(\mathbf{x}, \mathbf{x}_0)$ vanishes on Γ_2 and satisfies boundary condition (13). The boundary integral equation (24) holds only on γ_1 .

In the aforementioned problem formulation, the linear momentum equation is written in the Lagrangian description of motion, and Laplace's equation for the electric field in the Eulerian description of motion. De and Aluru [58] have written both equations in the Lagrangian description of motion, employed Newton's method to solve ODEs arising from the weak formulation of the problem and computed analytically the Jacobian matrix. This makes the resulting numerical algorithm computationally less intensive. However, one of our goals is to keep the FE formulation general enough to include a wide class of materials for the deformable electrode that makes the analytical evaluation of the Jacobian matrix impractical. We use LSODE with the Adam–Moulton method [63] to integrate the coupled nonlinear ODEs (23) that does not require the evaluation of the Jacobian matrix, and adjusts the time step adaptively to compute the solution within the prescribed absolute and relative tolerances.

3. Results and discussion

Based on the formulation given above, we have developed a computer code to find an approximate solution of the coupled nonlinear initial-boundary-value problem. It uses eight-node serendipity quadrilateral elements with 3×3 Gauss points for studying 2D structural problems and uses two-node line elements with one collocation point at the centroid of the element and 12 Gauss points for computing the electric flux $n(\mathbf{x}) \cdot \nabla\phi(\mathbf{x})$ on the boundary of the deformable electrode. Since, the BE has only one collocation point, the electric flux is constant over the element and is discontinuous across the inter element boundary. Therefore, discontinuities in the electric flux at sharp corners of the deformable electrode can be easily captured, as the variation of the electric flux over elements on both sides of a corner need not be continuous at the corner. Boundary elements with linear or quadratic variation of the electric flux need special treatment to capture discontinuities at a corner [64, 65], e.g. see discontinuous elements and corner problems in [66].

The mass matrix is lumped by using the special lumping technique. In LSODE, the relative and the absolute tolerances are set equal to 10^{-6} . Results for each problem are computed with at least two meshes to assess the order of error in the numerical solution. After every time step coordinates of nodes for the BE mesh are updated, the boundary integral equation (24) is solved for the electric flux $n(\mathbf{x}) \cdot \nabla\phi(\mathbf{x})$ along the boundary of the deformable electrode and surface tractions (15) due to the Coulomb pressure are computed and applied to surfaces of the deformable electrode. The FE and the BE codes are fully integrated into one software and no human intervention is needed.

3.1. Code verification

The code has been verified by comparing computed results for three problems with those obtained by numerically analyzing the same problems with commercial codes. The first problem studied is a $25 \mu\text{m}$ long, $10 \mu\text{m}$ wide and $0.5 \mu\text{m}$ thick fixed–fixed beam made of an isotropic neo-Hookean material with

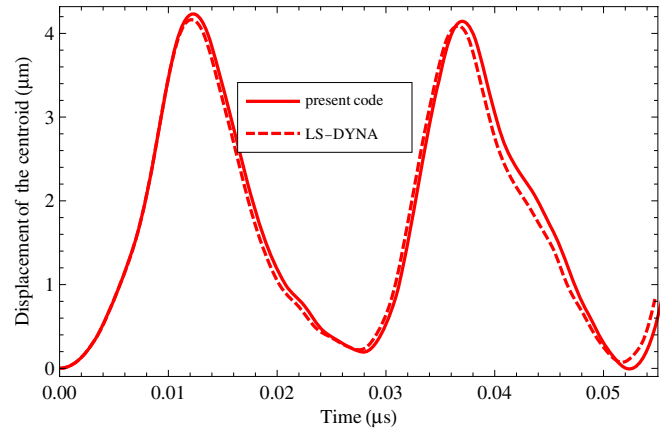


Figure 3. Time histories of the displacement u_3 of the centroid of the fixed–fixed beam under a body force $f_3 = 150 \text{ kN mm}^{-3}$.

$\rho_0 = 2231 \text{ kg m}^{-3}$, $\lambda = 12.05 \text{ GPa}$ and $\mu = 79.27 \text{ GPa}$. The magnitude 150 kN mm^{-3} of the body force is unusually high to induce large deformations in the beam so that effects of nonlinear strain–displacement relation (7) can be delineated. The computed results are compared with those derived by using the commercial FE software LS-DYNA by implementing in it the constitutive relation (6) through the user supplied subroutine option. Deformations of one-half of the beam have been studied due to the symmetry of the problem. The FE mesh for the plane strain problem has 60×10 eight-node serendipity elements along half of the length and the thickness of the beam. The element dimension along the beam length is varied gradually, and the element length at the fixed end of the beam is $1/5$ of that at the mid-span. A similarly graded 120×20 four-node FE mesh is employed to solve the problem with LS-DYNA. The FE mesh was successively refined to obtain converged solutions and results with only the finest mesh, described above, are given here. As can be seen from results plotted in figure 3, time histories of the centroidal deflection computed with our code agree very well with that obtained by using LS-DYNA. The variation of the E_{11} component of the Almansi–Hamel strain tensor, the e_{11} component of the Green–St Venant strain tensor defined by

$$e_{ij} = \frac{1}{2}(F_{li}F_{lj} - \delta_{ij}) \quad (26)$$

and the displacement u_3 along the beam span at $t = 0.0102 \mu\text{s}$ are exhibited in figure 4. It is clear that results computed with our code agree very well with those obtained with LS-DYNA. At points near the supports E_{11} and e_{11} exceed 0.2. However, along most of the beam span, the axial strain is about 0.01. Results from the Euler–Bernoulli beam theory will significantly under estimate the axial strain at points near the clamped edges.

The second problem analyzed is also a fixed–fixed $1000 \mu\text{m} \times 2.4 \mu\text{m} \times 30 \mu\text{m}$ ($L \times b \times h$) beam (cf figure 5) suspended $10.1 \mu\text{m}$ above a rigid electrode but we now compute the Coulomb pressure distribution due to the electric potential difference between the rigid electrode and the beam. For the silicon beam, we take $\rho_0 = 2231 \text{ kg m}^{-3}$, $\lambda = 97.5 \text{ GPa}$ and $\mu = 65.0 \text{ GPa}$. The domain Ω_2 is considered as vacuum with $\epsilon_0 = 8.854 \times 10^{-12} \text{ F m}^{-1}$, and the electric potential

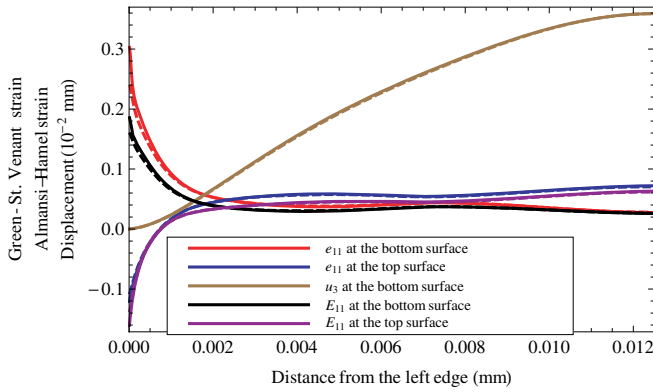


Figure 4. Variation of the Green–St Venant strain e_{11} and the Almansi–Hamel strain E_{11} along the top and the bottom surfaces of the beam, and of the displacement u_3 along the bottom surface of the beam at $t = 0.0102 \mu\text{s}$; results for only the left half of the beam are shown. Solid lines: present code, dashed lines: LS-DYNA.

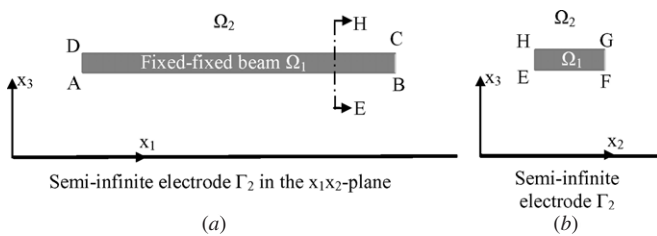


Figure 5. The long-section (a) and the cross-section (b) of the deformable electrode suspended over the rigid semi-infinite electrode.

difference between the two electrodes equals 10 V. The boundary of the long section of the beam is discretized using two different BE meshes, 60×4 and 3000×400 (elements along AB and CD \times elements along BC and DA). To model the exterior domain Ω_2 in the FE commercial code ANSYS, we use PLANE121 and INFIN110 elements (see figure 6). The values of r_0 and l_0 in figure 6 were gradually increased and the FE mesh was refined to obtain converged solutions. We compare in figure 7 the Coulomb pressure on edges AB, DC and BC of

the beam. As exhibited in figures 7(a) and (b), the electrostatic pressure distribution along AB and DC from our code agrees well with that from ANSYS except near the corners which could be due to the non-uniqueness of the unit normal at the corners. However, as shown in figure 7(c), mesh 1 failed to compute the Coulomb pressure distribution along the edge BC. Due to the very high aspect ratio ($AB/BC = 1000/2.4 \approx 417$), a finer BE mesh is required to compute the Coulomb pressure distribution on sides BC and DA of the beam. The distribution of the electrostatic pressure on the bottom surface AB and on the top surface CD of the beam is more important than that on edges BC and AD since it induces the downward electrostatic pressure which actuates the MEMS. Therefore, the BE meshes used here should suffice to compute the pull-in and the snap-through parameters of the MEMS.

Next, we compare in figure 8 the electrostatic pressure distribution on the boundary of a cross-section of the beam. The boundary of the cross-section of the beam is discretized using BE meshes consisting of 1000 elements along EF and GH and 100 elements along FG and HE. As exhibited in figures 8(a), (b) and (c), the electrostatic pressure distributions on EF, HG and FG from our code agree well with those from ANSYS except near the corners which could be due to the non-uniqueness of the unit normal at a corner. One can see that the electrostatic pressure along EF is not uniform because of the fringing fields due to the finite width and the finite height of the beam. The downward electrostatic pressure p_d per unit length of the beam can be computed by integrating the pressure along EF and HG. That is,

$$p_d = \text{Total Coulomb pressure along EF} - \text{Total Coulomb pressure along HG} = 0.151 \text{ Pa.} \quad (27)$$

If we neglect the fringing fields, then the pressure along the width EF of the beam is uniform and the downward pressure per unit length of the beam according to the PPA is given by

$$p_d = \frac{\epsilon b V^2}{2g_0^2} = 0.130 \text{ Pa,} \quad (28)$$

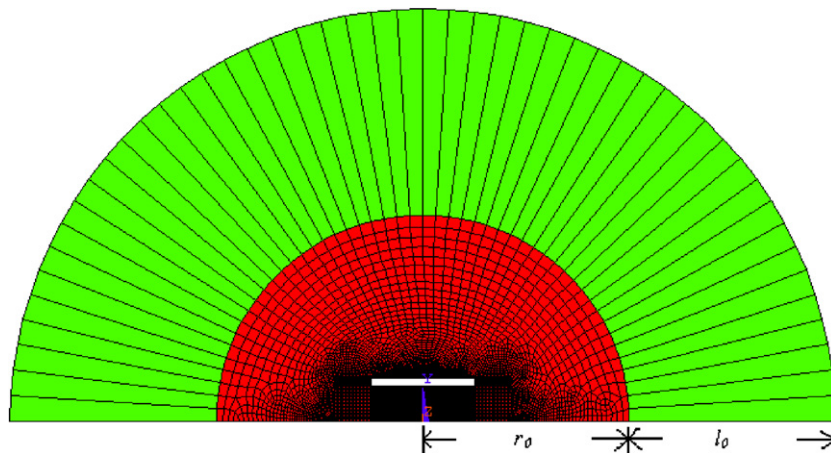


Figure 6. The mesh to study the electrostatic pressure on edges of the cross-section EFGH of the deformable electrode. PLANE121 elements in ANSYS are used to discretize the area (red, dark gray) around the deformable beam up to radius r_0 . Beyond the radius r_0 , INFIN110 elements (green, light gray) are used up to a length of l_0 to take into account the infinite extent of the domain Ω_2 ; $r_0 = 60 \mu\text{m}$ and $l_0 = 60 \mu\text{m}$ are used. Similarly, $r_0 = 2 \text{ mm}$ and $l_0 = 2 \text{ mm}$ are used in the analysis of the long section ABCD of the beam.

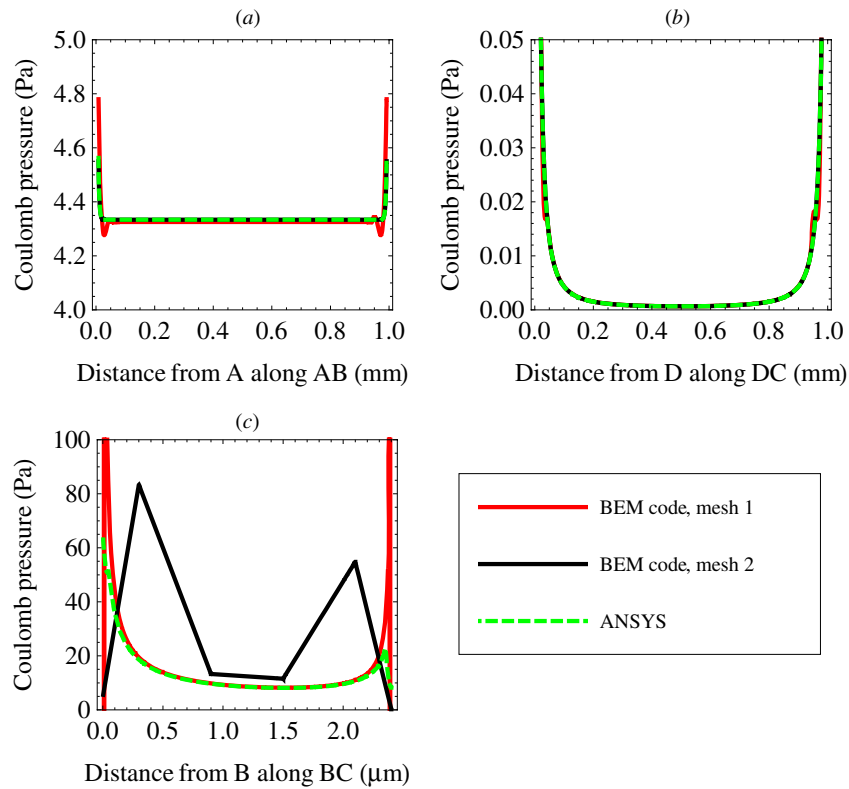


Figure 7. The Coulomb pressure distribution along boundaries AB, DC and BC of the beam (see ABCD in figure 5(a)); due to symmetry the electrostatic pressure distributions along BC and AD are the same.

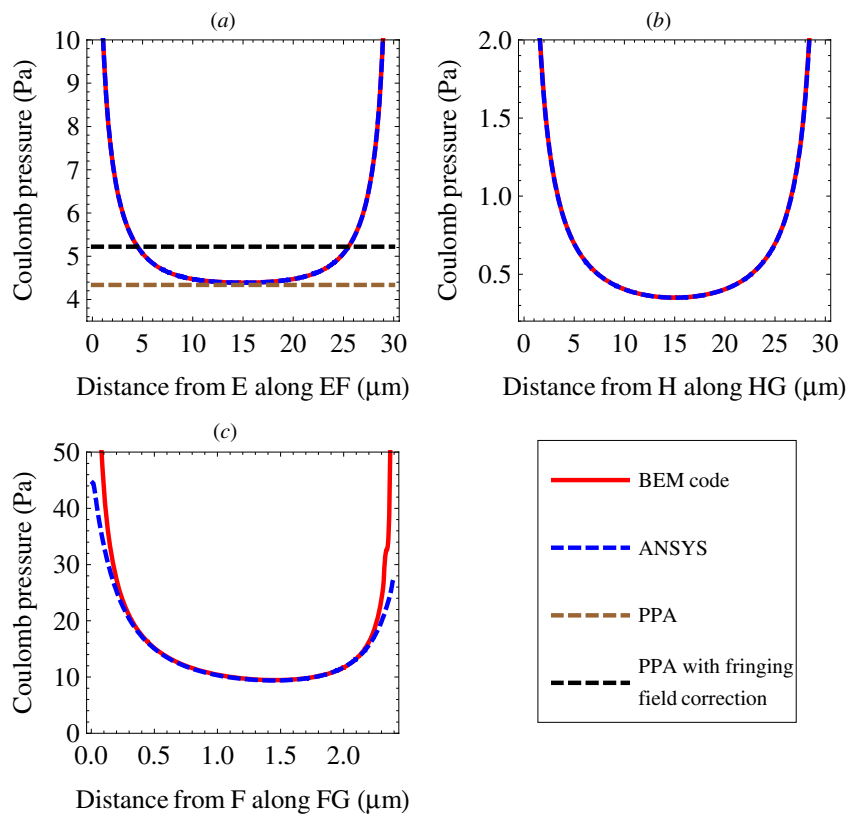


Figure 8. The Coulomb pressure distribution along the boundaries EF, HG and FG of the beam (see EFGH in figure 5(b)); due to symmetry the electrostatic pressure distributions along FG and HE are the same.

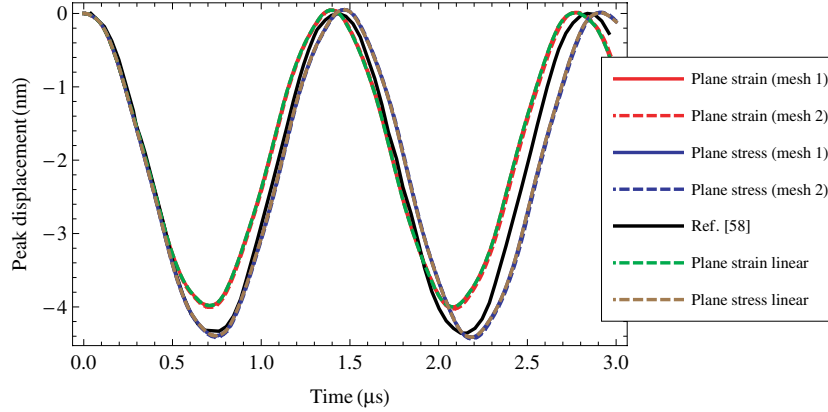


Figure 9. Time histories of the downward displacement of the centroid of the bottom surface of the fixed–fixed beam due to 2 V step potential difference between the rigid and the deformable electrodes. Plots of peak displacements from the linear and the nonlinear problems overlap.

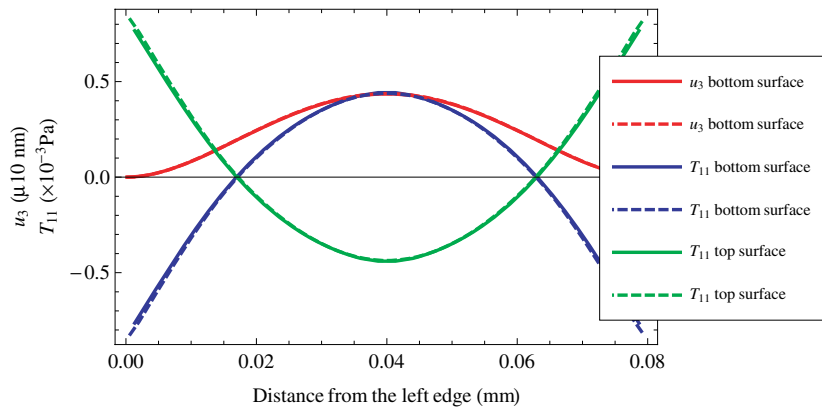


Figure 10. The variation of the Cauchy stress T_{11} and the displacement u_3 along the beam span at time $t = 0.7 \mu s$ due to 2 V step potential difference between the rigid and the deformable electrodes. Solid lines: mesh 1; dashed lines: mesh 2.

which is 14% less than the pressure obtained from the BEM solution. Therefore, for this case fringing fields cannot be neglected. The correction of the fringing fields according to the Mejis–Fokkema formula [12, 67] gives

$$p_d = \frac{\epsilon b V^2}{2g_0^2} \left(1 + 0.265 \left(\frac{g}{b} \right)^{3/4} + 0.53 \left(\frac{h}{b} \sqrt{\frac{g}{h}} \right) \right) = 0.157 \text{ Pa}, \quad (29)$$

which is about 3.7% more than that from the BE solution. Therefore, the beam problem can be analyzed as a 2D problem in the x_1x_3 plane with acceptable errors if the electrostatic pressure found from the PPA is corrected with the Mejis–Fokkema formula.

Next, we study transient deformations of a fixed–fixed $80 \mu m \times 0.5 \mu m \times 10 \mu m$ silicon beam suspended $0.7 \mu m$ above a flat rigid electrode due to a step electric potential difference applied to the two electrodes. This problem has been studied in [58] as a plane stress problem. However, as the ratio of the width to the height of the beam is 20, it should be considered as a plane strain problem. Here, we analyze it as both plane stress and plane strain problems to delineate differences between the two sets of results. Since, $g_0/b = 0.07$ and $h/b = 0.05$, fringing fields can be neglected [39].

To demonstrate the effect of the nonlinearity in the strain–displacement relation (7), we also study the problem with the linear strain–displacement relation:

$$\hat{E}_{ij} = \frac{1}{2}(u_{i,j} + u_{j,i}). \quad (30)$$

Two FE meshes, 30×4 and 60×8 (number of elements along the length and the thickness respectively), with 136 and 272 BEs, respectively, are used to solve the 2D problem. Figure 9 exhibits the time history of the downward displacement of the centroid of the bottom surface of the beam for an applied step electric potential difference of 2 V between the beam and the rigid electrode; results from our code for the plane stress problem agree well with those reported in [58]. The maximum transverse displacement and the time period of oscillations from the plane strain analysis are about 10% less than those from the plane stress analysis. The nonlinearity in the strain–displacement relation has a negligible effect on both the amplitude and the time period of oscillations. Figure 10 shows the variation of the Cauchy stress T_{11} along the span of the beam at $0.7 \mu s$. As the two meshes give virtually the same results, for subsequent analyses we use the first mesh. The magnitude of the axial stress near the fixed edges of the beam is more than twice of that at the midsection of the beam.

Figure 11 depicts the downward displacement of the centroid of the bottom surface of the beam versus time

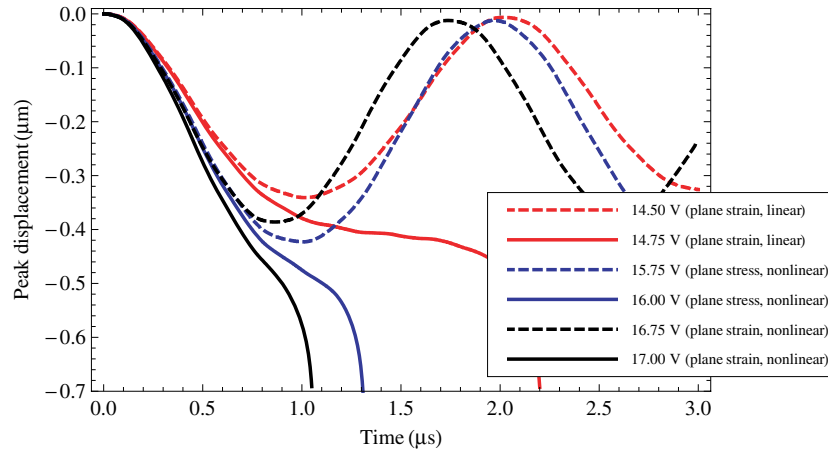


Figure 11. Time histories of the deflection of the centroid of the bottom surface of the fixed-fixed beam for different step applied electric potentials from the nonlinear and the linear strain-displacement relations.

due to different applied step voltages. For the plane strain problem with the nonlinear strain-displacement relation, the pull-in voltage is between 16.75 V and 17.0 V since for the 16.75 V potential difference, the peak deflection stays bounded but for the 17.0 V potential difference it becomes unbounded. By solving the problem for several values of the potential difference between 16.75 V and 17.0 V, one can compute a better value of the pull-in voltage. For the plane stress approximation with the nonlinear strain-displacement relation, the pull-in voltage is found to be between 15.75 V and 16.00 V. The pull-in voltage for the plane stress problem reported in [58] is 15.7 V. For the plane strain approximation with the linear strain-displacement relation, the pull-in voltage is between 14.5 V and 14.75 V. The analysis with the linear strain-displacement relation underestimates the pull-in voltage by 8%. For the plane strain problem, the consideration of the nonlinear strain-displacement relation increases the absolute maximum displacement before the pull-in instability to $0.39 \mu\text{m}$ ($=0.55 g_0$) from $0.34 \mu\text{m}$ ($=0.48 g_0$) obtained from the analysis of the linear problem. Using a spring-mass model, the maximum pull-in displacement for a statically loaded micro-beam equals $0.33 g_0$ [7]. The spring-mass model neither accounts for the nonlinear strain-displacement relation nor the actual distribution of the Coulomb pressure. Tilmans and Legtenberg [35] accounted for the actual deflection distribution but neglected nonlinear mid-plane stretching of the micro-beam and obtained a pull-in displacement of $0.4 g_0$ in a static problem. Using a reduced-order model, Abdel-Rahman *et al* [36] showed that the pull-in displacement equals $0.39 g_0$ in a static problem if both the mid-plane stretching and the actual distribution of the Coulomb pressure are considered.

3.2. Fixed-fixed beam as MEMS

In order to compare the pull-in parameters of a beam with those of an arch in the next subsection, we study transient deformations of a fixed-fixed silicon beam of length = 1 mm, width = $30 \mu\text{m}$ and height = $2.4 \mu\text{m}$, initial gap = $10.1 \mu\text{m}$. For a step potential difference of 90 V, the 30×2 and $50 \times$

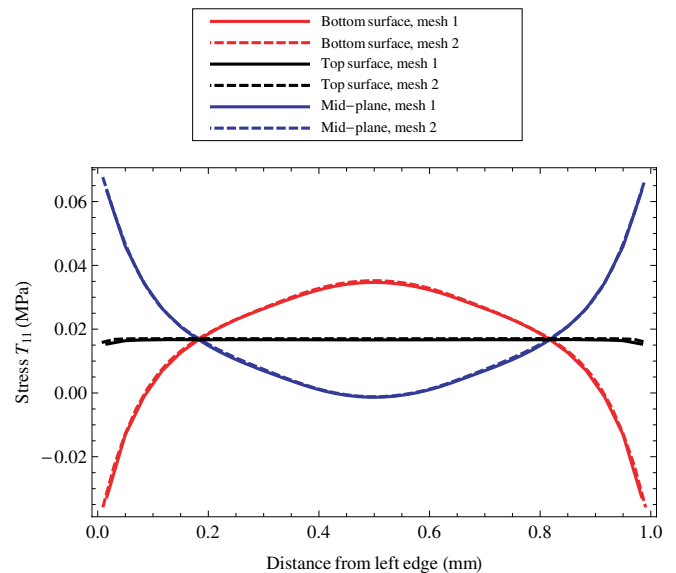


Figure 12. Variation of the Cauchy stress T_{11} along the beam span at time $t = 15 \mu\text{s}$ due to 90 V step potential difference between the rigid and the deformable electrodes.

4 FE meshes (elements along the length and the thickness directions, respectively) with 128 and 216 BEs gave maximum downward displacements of the centroid of the bottom surface equal to 6.188 and $6.247 \mu\text{m}$, respectively. The variation of the Cauchy stress T_{11} along the span of the beam at time $t = 15 \mu\text{s}$ is exhibited in figure 12. It is clear that the two FE meshes give virtually the same stresses, and for subsequent analyses, we use the first mesh. Whereas the distribution of axial stress T_{11} on the midsurface of the beam is nearly uniform and equals ~ 0.015 MPa, the magnitude of T_{11} at points on the top and the bottom surfaces that are near the clamped edges equal ~ 0.07 and ~ 0.04 MPa, respectively. Furthermore, distributions of T_{11} on the top and the bottom surface are not uniform.

Krylov *et al* [20] have studied static deformations of this beam both experimentally and numerically with a reduced-order model, and their values of the pull-in voltage are 100.0 V

Table 1. Pull-in parameters for the fixed–fixed beam for different rates of the applied potential difference

Rate of applied potential difference ($V \mu s^{-1}$)	Nonlinear problem		Linear problem	
	The pull-in voltage (V)	The pull-in displacement (μm)	The pull-in voltage (V)	The pull-in displacement (μm)
Step load	99.50	7.7	49.0	4.5
0.60	116.50	7.0	65.1	7.5
0.24	114.25	6.6	59.0	5.6
0.17	113.75	6.5	58.0	5.5
0.12	113.50	6.4	57.0	5.3
0.06	113.00	6.4	56.0	5.3
Experiment	100.00	5.0		
ROM ^a (static problem)	118.50	6.5		

^a Reduced-order model.

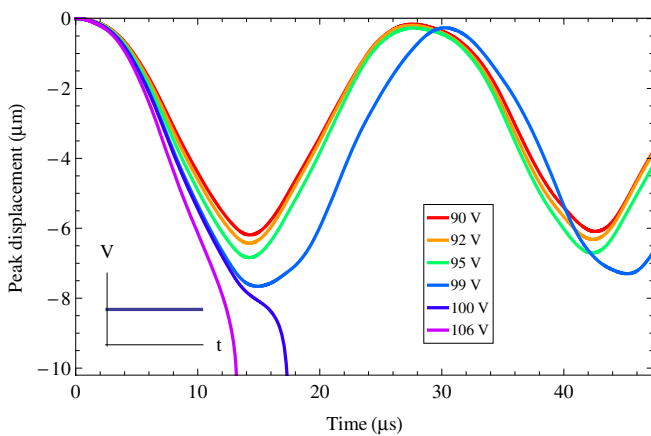


Figure 13. Time histories of the deflection of the centroid of the bottom surface of the fixed–fixed beam for different values of the step electric potentials from analysis of the nonlinear problem.

and 118.5 V, respectively. Figure 13 exhibits the peak downward deflection of the centroid of the beam bottom surface due to different step potential differences. The pull-in voltage for the dynamic problem is found to be between 99.0 V and 100.0 V since for the 99.0 V potential difference, the peak deflection stays bounded but for the 100.0 V potential difference, it becomes unbounded. By solving the problem for several values of the potential difference between 99.0 V and 100.0 V, one can compute a better value of the pull-in voltage. We note that the presently computed pull-in voltage is very close to Krylov *et al*'s [20] experimental value. The pull-in voltage is found to be between 49.0 V and 50.0 V from the analysis of the linear problem and is nearly one-half of that for the nonlinear problem. Thus, assumption of the linear strain–displacement relation gives the pull-in voltage equal to one-half of that obtained with the nonlinear strain–displacement relation. We note that the difference in the pull-in voltage from the linear and the nonlinear strain–displacement relations are problem specific; for the $80 \mu m \times 0.5 \mu m \times 10 \mu m$ beam studied above, the difference in the two pull-in voltages was only 12%. The pull-in displacements for the $80 \mu m \times 0.5 \mu m \times 10 \mu m$ and the $1000 \mu m \times 2.4 \mu m \times 30 \mu m$ beams equal $0.78 h$ and $3.25 h$, respectively.

To delineate the effect of the rate of loading on the pull-in parameters, we increase the electric potential difference

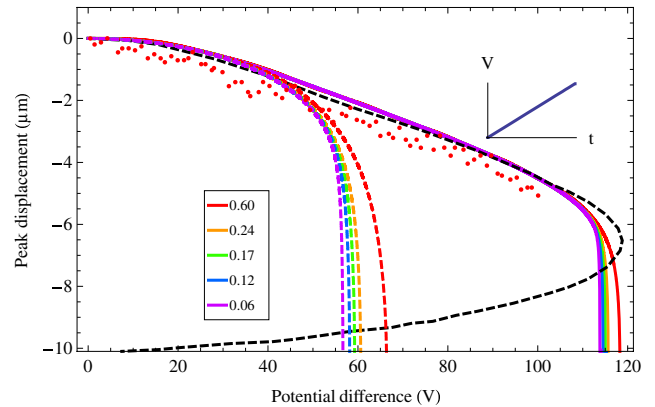


Figure 14. The deflection of the centroid of the bottom surface of the fixed–fixed beam versus the applied voltage for different rates ($V \mu s^{-1}$) of increase of the voltage. Red dots represent experimental data from [12] for static deformations of the beam, and the black dashed line is the bifurcation curve reported in [12]. Solid and dashed lines correspond, respectively, to results from analyses of the nonlinear and the linear problems.

between the beam and the rigid electrode linearly with time. Figure 14 shows the peak deflection of a point of the beam versus the applied voltage for different rates of increase of the applied voltage. Experimental data and the bifurcation curve derived with a reduced-order model [12] are also exhibited. As summarized in table 1, the pull-in voltage and the pull-in deflection decrease with a decrease in the rate of increase of the potential difference. The pull-in voltage increases by 2.7% with a tenfold increase in the rate of increase of V from $0.06 V \mu s^{-1}$ to $0.6 V \mu s^{-1}$. However, there is about 16% decrease in the pull-in voltage when the applied potential difference is changed from linearly varying to a step load. The pull-in voltage of 113 V for the slowest loading rate considered is about 13% more than the experimental static pull-in voltage and about 4.6% less than the numerical static pull-in voltage reported in [12, 67] with a reduced-order model and the Coulomb pressure given by the PPA with the fringing field correction. The present work finds the Coulomb pressure from the charge distribution of the electric field and applies it along the normal to the bounding surface in the deformed configuration. For both step and linearly increasing potential difference, the use of the linear strain–displacement relation

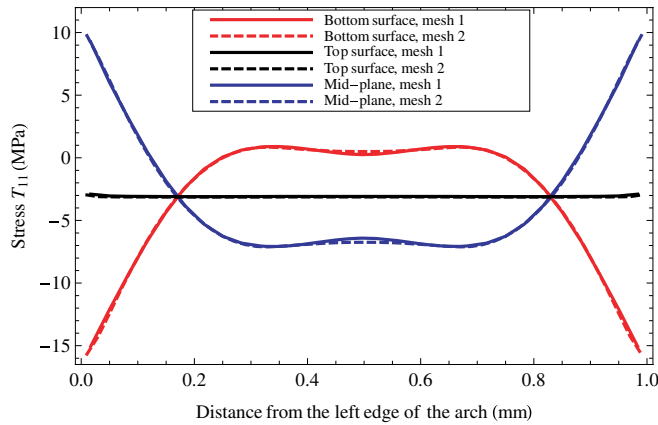


Figure 15. The Cauchy stress T_{11} along the span of the arch at the top, the bottom and the mid-plane at time $t = 20 \mu\text{s}$ due to 60 V potential difference from the analysis of the plane strain nonlinear problem.

underestimates the pull-in voltage by about 50% and the pull-in deflection by as much as 70%.

3.3. Transient deformations of a bell-shaped arch MEMS

Referring to figure 1, we consider a bell-shaped silicon arch with base length $L = 1 \text{ mm}$, width $b = 30 \mu\text{m}$, thickness $h = 2.4 \mu\text{m}$, initial gap $g_0 = 10.1 \mu\text{m}$, the arch rise $H = 3.0 \mu\text{m}$ and its bottom-surface described by $z_0(x_1) = H \sin^2(\pi x_1/L)$. Values assigned to material parameters are the same as those for the beam of the last section. We analyze it as a plane strain problem and consider the effect of fringing fields by increasing the traction T_i^0 (cf equation (15)) on the bottom surface of the arch due to the electrostatic force by a factor of

$$\left(1 + 0.265 \left(\frac{z_0(x_1) + g_0(x_1) + w(x_1)}{b}\right)^{3/4} + 0.53 \left(\frac{h}{b} \sqrt{\frac{z_0(x_1) + g_0(x_1) + w(x_1)}{h}}\right)\right) \quad (31)$$

in accordance with the Mejis–Fokkema formula [12, 67].

For a step potential difference of 60 V, the two 30×2 and 50×4 FE meshes (elements along the length and elements along the thickness directions, respectively) with 128 and 216 BEs gave maximum downward displacements of the centroid of the bottom surface equal to 1.657 and 1.677 μm . The variations along the span of the arch of the Cauchy stress T_{11} on the top, the middle and the bottom surfaces at time $t = 20 \mu\text{s}$ are exhibited in figure 15. It is clear that the two FE meshes give virtually the same stresses, and for subsequent analyses, we use the first mesh. As for the beam, the maximum values of $|T_{11}|$ occur at points near the clamped edges, whereas T_{11} is essentially uniform on the midsurface of the arch and equals $\sim -3 \text{ MPa}$, that at the edges equals $\sim -16 \text{ MPa}$ on the bottom surface and $\sim 10 \text{ MPa}$ on the top surface. Because of the curvature of the undeformed arch, maximum magnitudes of the compressive and the tensile axial stress are different.

Figure 16 displays the peak displacement of the centroid of the bottom surface of the arch versus the applied voltage

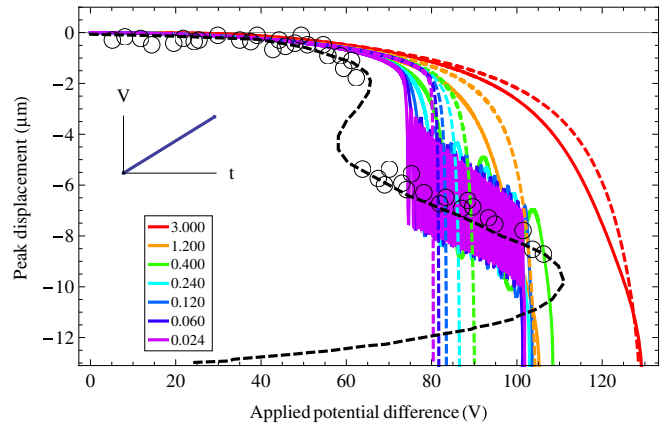


Figure 16. For different rates ($V \mu\text{s}^{-1}$) of increase of the potential difference, the downward displacement of the centroid of the bottom surface of the fixed–fixed bell-shaped arch versus the applied potential difference. Black circles correspond to data from static experiments [12], and the black dashed line is the corresponding bifurcation curve reported in [12]. Solid and dashed lines correspond, respectively, to analysis of the nonlinear and the linear problems.

for different uniform rates of increase of the electric potential. Results from the analysis of the linear problem, experimental data [12] and the bifurcation curve derived with a reduced-order model in [12] are also exhibited. The first sudden increase in the peak displacement from the analysis of the nonlinear problem at the potential difference of $\sim 75 \text{ V}$ corresponds to the snap-through instability of the arch. For low to medium rates of increase of the applied potential difference (i.e. $\leq 0.4 \text{ V } \mu\text{s}^{-1}$), the arch vibrates around the snapped-through shape till the applied potential difference reaches the pull-in voltage of $\sim 102 \text{ V}$. For the loading rates of 1.2 and 3.0 $\text{V } \mu\text{s}^{-1}$, the snap-through instability is not observed, and only the pull-in instability occurs at $\sim 105 \text{ V}$ and $\sim 129 \text{ V}$, respectively. We have summarized in table 2 the snap-through and the pull-in parameters for different rates of loading. As the rate of increase of the potential difference is decreased the snap-through voltage gradually decreases to 73 V monotonically; however, the pull-in voltage approaches 111 V non-monotonically. It is evident that the response of the arch approaches that of the statically deformed arch as the rate of loading is decreased. Krylov *et al* [12] have studied static deformations of the arch experimentally and numerically by using a reduced-order model. Their experimental snap-through voltage of 62.3 V differs by 5% from their numerically computed voltage of 65.7 V, and the corresponding pull-in voltages are 106 V and 111 V. For a step load the present analysis gives 65 V and 92 V, respectively, for the snap-through and the pull-in voltages. We note that the loading rate in experiments cannot be accurately determined. Analyses with the linear strain–displacement relation fail to predict the snap-through instability. Therefore, the nonlinearity in the strain–displacement relation must be considered for studying the snap-through instability. For subsequent problems, results from analyses with the nonlinear strain–displacement relation are reported.

Table 2. The snap-through and the pull-in parameters for the fixed–fixed bell-shaped arch for different rates of applied potential difference from the analysis of the nonlinear problem.

Rate of applied potential difference ($V \mu s^{-1}$)	The snap-through instability		The pull-in instability	
	Voltage (V)	Displacement (μm)	Voltage (V)	Displacement (μm)
Step load	65.0	2.6	92.0	11.0
3.000	–	–	123.0	11.0
1.200	–	–	100.0	6.0
0.400	77.5	2.0	111.5	9.0
0.240	75.5	1.9	111.0	8.0
0.120	74.0	1.8	113.0	9.0
0.060	73.5	1.7	111.0	8.0
0.024	73.0	1.7	116.0	8.5
Experiment	62.3		106.0	
ROM (static problem)	65.7		111.0	

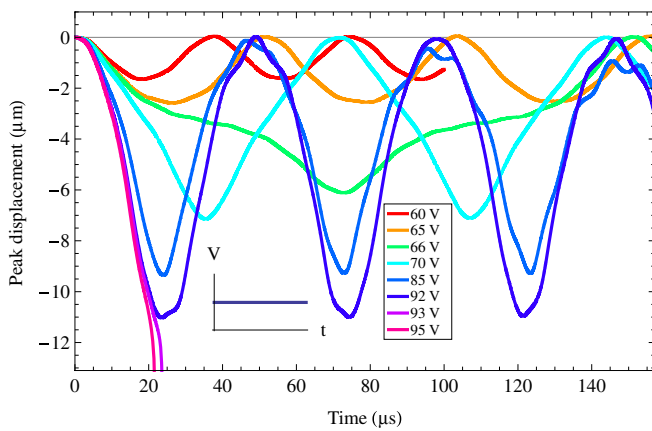


Figure 17. Time histories of the downward displacement of the centroid of the fixed–fixed bell-shaped arch for different applied step voltages.

Figure 17 shows time histories of the deflection of the arch for different values of the applied step potential difference. A significant difference in the response of the arch occurs when the applied potential difference is increased from 65 V to 66 V in that the amplitude and the time period of oscillations increase noticeably. This sudden change in the response due to a small change in the applied potential difference indicates the snap-through instability. It should also be evident from the plot of the peak displacement versus the applied step voltage shown by the red curve in figure 18. The pull-in voltage is found to be 92 V which is nearly 40% more than the snap-through voltage. The snap-through and the pull-in voltages due to step electric potentials are lower by 15% and 20%, respectively, than those due to a linearly increasing electric potential of $0.024 V \mu s^{-1}$; we recall that the pull-in voltage for the beam studied above exhibits the same trends.

Since the rise parameter, e_{arch} , for the shallow arch is 4.33, according to the criterion given in [33], it should not experience a snap-through instability under a deflection-independent distributed static or transient mechanical load. However, under the step electric potential difference which induces a deflection-dependent distributed force, the arch experiences the snap-through instability. Therefore, the

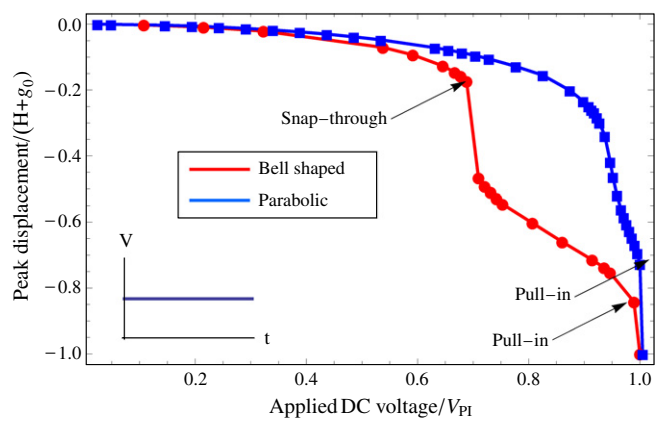


Figure 18. The maximum absolute deflection of the centroid of the bottom surface of the fixed–fixed bell-shaped and parabolic arches for different applied step voltages.

criterion developed with the assumption of displacement-independent loads does not apply for displacement-dependent (or follower type) loads.

3.4. Transient deformations of a parabolic arch MEMS

The parabolic arch studied in this subsection differs from the bell-shaped arch analyzed above primarily in the nonzero slopes of the parabolic arch at the two fixed edges and zero slopes for the bell-shaped arch. The geometric and material parameters of the parabolic arch are $L = 500 \mu m$, $b = 50 \mu m$, $h = 2.6 \mu m$, $H = 2.9 \mu m$ and $g_0 = 6.4 \mu m$ (see figure 1); $\rho_0 = 2310 \text{ kg m}^{-3}$, $\lambda = 73.95 \text{ GPa}$ and $\mu = 63.0 \text{ GPa}$. Since the average gap to the width ratio $(H/2 + g_0)/b$ of 0.157 and h/b of 0.052 is less than 0.5, effects of fringing fields can be neglected [39]. Even though, in [39] an initially flat beam is considered, for the present problem, the arch height is negligible as compared to its width and length, and neglecting fringing fields should not introduce an appreciable error in the pull-in parameters. We analyze it as a plane strain problem. The 20×3 and the 40×4 FE meshes with 92 and 176 BEs gave the maximum centroidal deflections of 0.442 and $0.444 \mu m$ for 110 V step potential difference. Variations of

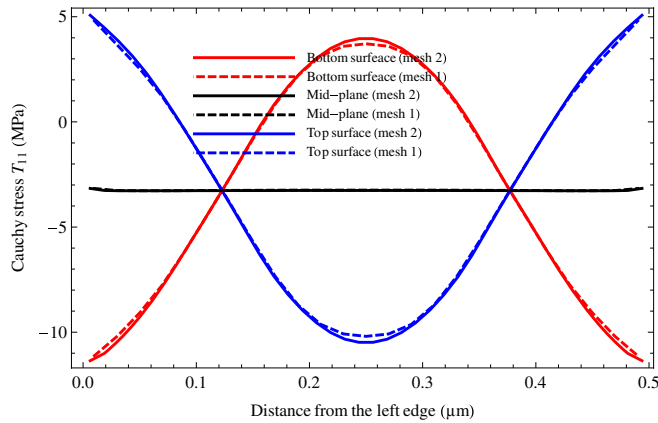


Figure 19. At $t = 4 \mu s$, the variation of the Cauchy stress tensor T_{11} along the span of the arch on the top, the bottom and the mid-plane due to 110 V step potential difference.

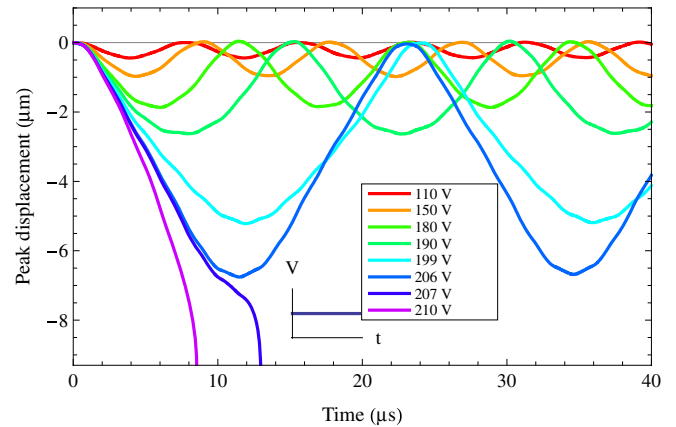


Figure 21. Time histories of the peak downward displacement of the centroid of the fixed-fixed parabolic arch for different applied step voltages.

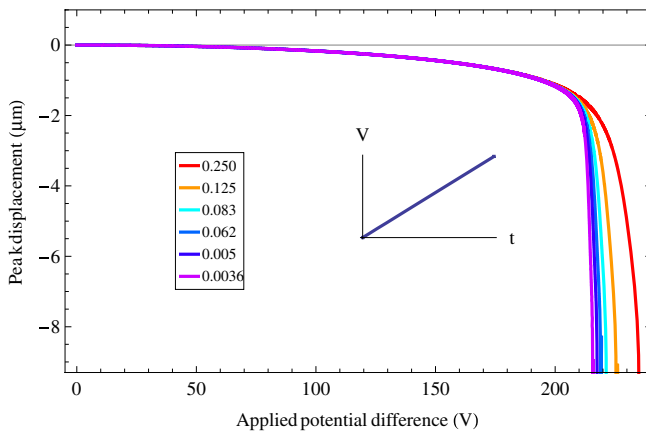


Figure 20. For different rate of increase in the applied potential difference ($V \mu s^{-1}$) the downward displacement of the centroid of the bottom surface of the fixed-fixed parabolic arch versus the applied voltage.

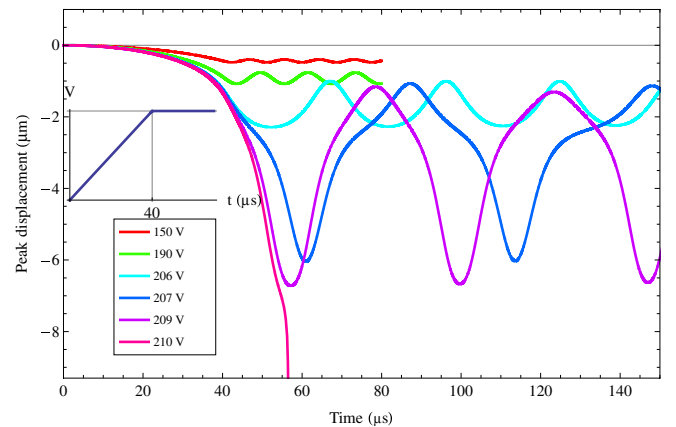


Figure 22. Time histories of the peak downward displacement of the centroid of the parabolic arch for different values of the steady potential difference.

the Cauchy stress T_{11} along the span of the beam at time $t = 4 \mu s$ are exhibited in figure 19. As results are virtually the same from the two meshes, for the subsequent analyses we use the first mesh.

Figure 20 evinces time histories of the peak deflection of the centroid of the bottom surface of the arch for different uniform rates of increase of the electric potential. A sudden increase in the peak displacement, observed for a potential difference of 210 V, signifies the pull-in instability. The pull-in voltage depends weakly upon the rate of increase of the applied potential difference. No snap-through instability is observed. Recall that for the bell-shaped arch both instabilities were found.

For different step potential difference, figure 21 exhibits the downward displacement of the centroid of the bottom surface of the arch versus time. Unlike for the bell-shaped arch, the amplitude of vibration increases gradually with the increase in the applied step voltage till the potential difference equals 206 V. A sudden change in the response occurs when the applied step voltage is increased to 207 V; thus the dynamic pull-in voltage is between 206 V and

207 V. The blue line in figure 18 shows the variation of the peak downward displacement with the applied step potential difference. Unlike the bell-shaped arch, no sudden change in the peak displacement is seen other than the one at the pull-in voltage. Therefore, the snap-through instability did not occur under step loading also. We note that dimensions of the sinusoidal and the bell-shaped arches are different.

For the applied voltage increased linearly from zero to the desired value in $40 \mu s$, and then held there, figure 22 shows time histories of the downward displacement of the centroid of the bottom surface of the arch for various values of the steady voltages. A noticeable difference in responses of the arch for applied steady potential differences of 206 V and 207 V is found. For 207 V, the arch oscillates with larger amplitude (see figure 23) and larger time period than those for 206 V. This sudden change in the response of the arch due to a small change in the applied potential difference indicates the snap-through instability. The pull-in voltage is found to be 210 V. We recall that no snap-through instability occurred for this arch under both a step potential difference and a linearly increasing potential difference.

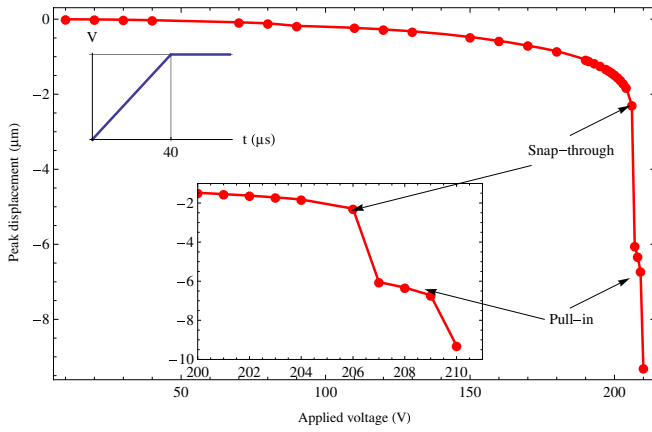


Figure 23. The maximum downward displacement of the centroid of the bottom surface of the fixed–fixed parabolic arch versus different applied ramp voltages. Two jumps in the displacement are observed. The first jump at 206 V corresponds to the snap-through instability and the second jump at 209 V corresponds to the pull-in instability.

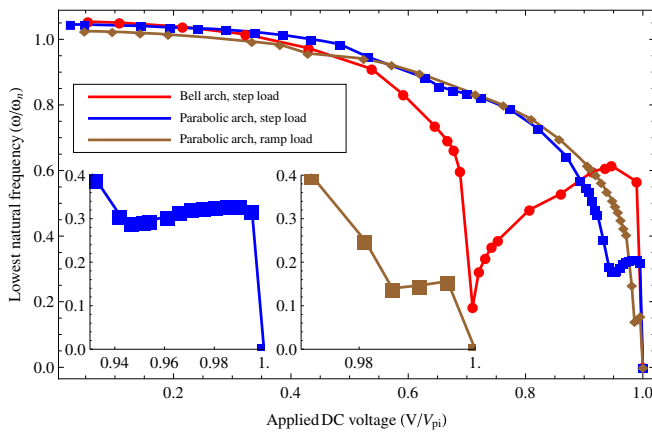


Figure 24. The lowest natural frequency versus the electric potential difference for the fixed–fixed parabolic and bell-shaped arches.

3.5. Variation of the lowest natural frequency of arch MEMS with applied voltage

The natural frequency of a MEMS device is an important parameter as it indicates its stiffness, and it affects the quality factor and the switching time. The lowest natural frequencies, ω , 37.9 kHz and 136.8 kHz, of the bell-shaped and the parabolic arches, respectively, deformed by a potential difference of 5 V are very close to their natural frequencies, ω_n , 36.0 and 135.5 kHz obtained from a converged modal analysis of the undeformed arches with the commercial FE code ANSYS. Figure 24 shows the variation of the lowest natural frequency (ω/ω_n) with the applied step voltage (V/V_{pi}), where V_{pi} is the pull-in voltage from the analysis of the dynamic problem. With an increase in the deformation of the arches due to an increase in the applied potential difference, the lowest natural frequencies of the deformed arches decrease gradually. This decrease in the lowest natural frequency can be explained with the Mises truss model [58, 20]. The nondimensional electrostatic force between the deformable and the rigid electrodes with the PPA is given by [12]:

$$F_e = \frac{\beta}{(1-w)^2}. \quad (32)$$

Here, w is the ratio of the peak displacement of the deformable electrode to the initial gap, and β is the nondimensional potential difference parameter between the two electrodes. For $w < 1$, using the Binomial theorem, we get

$$F_e = \beta(1 + 2w + 3w^2 + 4w^3 + \dots). \quad (33)$$

For relatively small voltages and hence small displacements, the electrostatic pressure F_e depends only on β ; however, as β increases, w also increases, and F_e depends on w and β . This makes F_e a negative spring, which decreases the natural frequency, and this effect is known as the electrostatic softening [36]. However, as β increases, so does w , and the strain hardening due to nonlinearities in the strain–displacement relation compensates for the electrostatic softening.

An examination of values of the maximum Green–St Venant principal strain, E^{Pr} , plotted in figures 25–27 on the deformed shapes of the arches at different applied step potential differences provides a qualitative explanation of the strain hardening effect. For the bell-shaped arch, as indicated in figure 25, at the potential difference of 65 V ($V/V_{pi} = 0.69$), E^{Pr} in an extreme shape of the arch equals 0.008% which is too small for nonlinearities in the strain–displacement relation to have a noticeable effect. Therefore, the electrostatic softening effect dominates the strain hardening effect. The natural frequency declines sharply at 66 V due to the snap-through instability. Under a potential difference greater than 65 V, the arch oscillates with $E^{Pr} = 0.014\%$ and 0.02% at 66 V and 92 V, respectively. Hence, after the snap-through the lowest natural frequency increases because hardening due to stretching of the arch compensates for the electrostatic softening. However, the lowest natural frequency again suddenly falls to zero at the pull-in voltage of 92 V when the softening and the hardening effects cancel each other.

For the parabolic arch deformed by a step potential difference, the lowest natural frequency also decreases initially. As the snap-through instability does not occur in this arch under a step electric potential difference, the lowest natural frequency does not drop sharply; cf figure 24. Instead as the arch oscillates with increasing amplitude, the strain hardening effect gradually compensates the electrostatic softening and the lowest natural frequency starts to increase. The E^{Pr} for 130 V ($V/V_{pi} = 0.62$) step electric potential difference equals 0.005%, which increases to 0.04% at 196 V ($V/V_{pi} = 0.96$) (see figure 26). For higher potential differences, the arch gets inverted during its oscillations. By examining shapes of the arch at 196 V (see figure 28(a)), we found that the equilibrium shape of the arch is about to invert, which means that the arch oscillates in the inverted shape only during at most half of the vibration cycle. We define the equilibrium shape of the arch as the one in which the downward velocity of the centroid is the maximum. However, for a potential difference higher than 196 V (see figure 28(b)), the equilibrium shape of the arch also inverts, which indicates that the arch is in the inverted shape during more than half of the vibration cycle. Thus, the arch experiences a higher

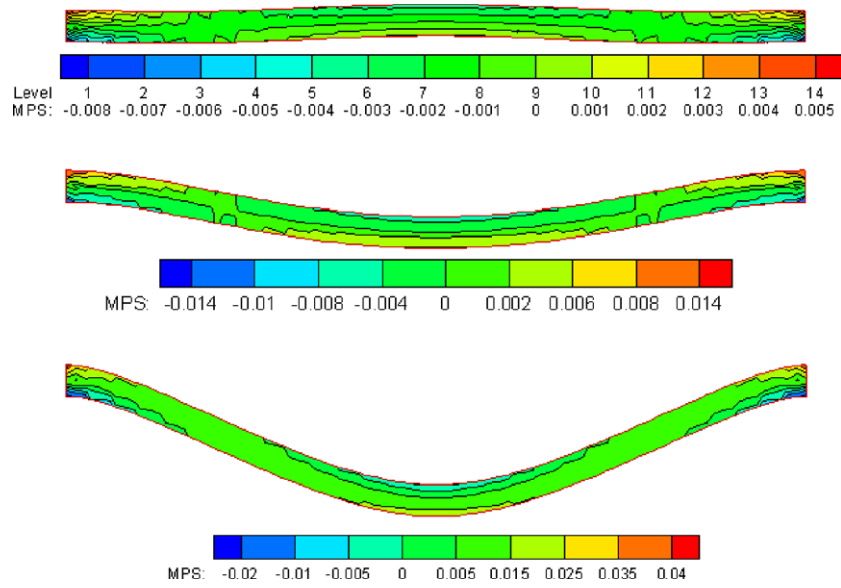


Figure 25. The maximum principal Green–St Venant strain (MPS in %) on the extreme deformed shapes of the bell-shaped arch for the three values of the applied step potential differences. Top: 65 V; middle: 66 V and bottom: 92 V.

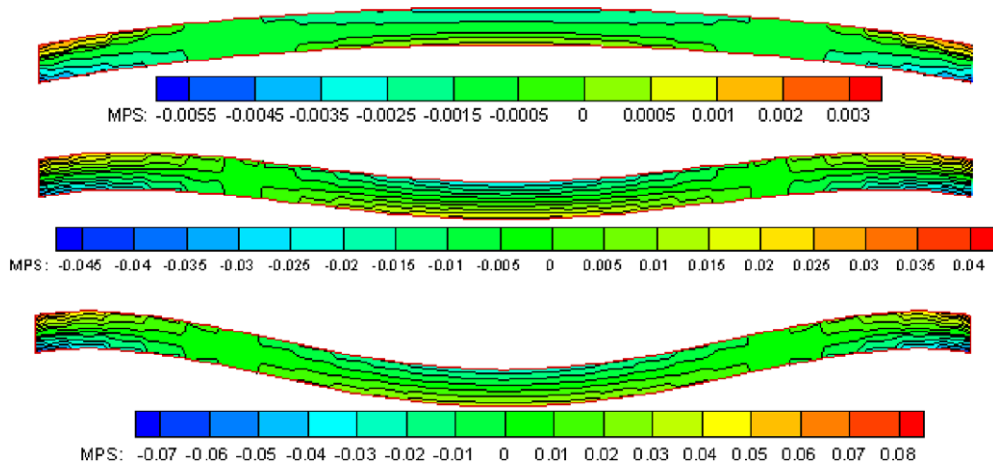


Figure 26. The maximum principal Green–St Venant strain (in %) on the extreme deformed shapes of the parabolic arch for the three values of the applied step potential differences. Top: 130 V; middle: 196 V and bottom: 205 V.

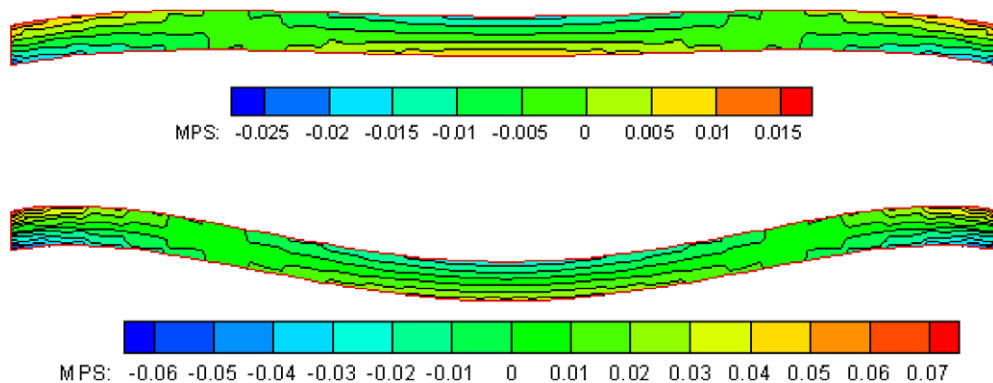


Figure 27. The maximum principal Green–St Venant strain (in %) on the extreme deformed shapes of the parabolic arch for the two values of the applied ramp potential difference. Top: 206 V and bottom: 207 V.

level of strain during most part of the cycle (see figure 26). Therefore, during deformations of the arch for a step potential difference between 196 V and 206 V, the strain hardening

dominates the electrostatic softening and the lowest natural frequency increases. However, the lowest natural frequency again suddenly falls to zero at the pull-in voltage of 207 V.

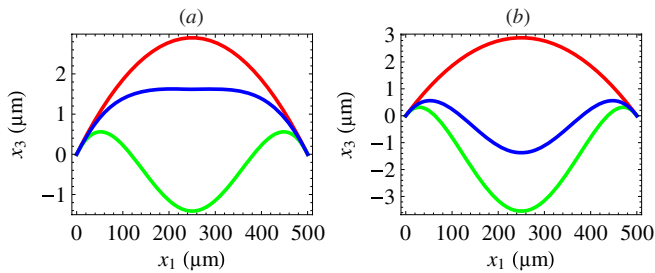


Figure 28. Two extreme and one intermediate shapes of the parabolic arch for the two values of the potential difference: (a) 196 V and (b) 205 V.

When the parabolic arch is loaded with the electric potential varying linearly from zero to a steady value in $40 \mu\text{s}$, we observe the snap-through instability. In this case, the lowest natural frequency of the arch decreases sharply at 207 V due to the snap-through instability. As indicated in figure 27, the E^{Pr} increases from 0.025% before the snap-through to 0.06% after the snap-through. Hence, after the snap-through, the lowest natural frequency increases because hardening due to stretching of the arch exceeds softening due to the Coulomb pressure. However, the lowest natural frequency again suddenly falls to zero at the pull-in voltage when the structural stiffness drops to zero.

The sharp drop in the lowest natural frequency of the arch at the snap-through and the pull-in instabilities agrees with the observation that the lowest natural frequency of the arch becomes zero at bifurcation points C and F in figure 2.

3.6. Discussion

Results for the fixed–fixed beam (cf section 3.2) and the two arches (cf sections 3.3 and 3.4) indicate that for the step loading inertia effects cannot be neglected. The pull-in voltage of the fixed–fixed beam equals 99.5 V under the step load and 113.0 V for the slowest rate of increase of the potential difference. The snap-through and the pull-in voltages of the bell-shaped arch equal 65 V and 92 V, respectively, under the step load and 73 V and 116 V, respectively, for the slowest rate of increase of the potential difference (cf table 2). The pull-in voltages of the fixed–fixed parabolic arch equal 207 V and 215 V, respectively, under the step load and the slowest rate of increase of the potential difference. The bell-shaped arch experiences the snap-through instability under both slowly and rapidly applied potential differences. However, the parabolic arch exhibits the snap-through instability only when the potential difference is increased linearly from zero to a steady value in $40 \mu\text{s}$ and subsequently held constant. Whether or not an arch exhibits the snap-through instability depends on a number of parameters, such as the ratio of the arch thickness to the arch rise [33], the angle of the arch at the fixed end (for of a circular and a parabolic arch) [22], the ratio of the arch thickness to the maximum distance from the flat rigid electrode and the rate of increase of the applied potential difference. Finding a phase diagram that shows values of parameters for which the snap-through instability occurs is not easy.

We have neglected the effect of damping. The damping coefficient of a MEMS device is determined by several variables such as the pressure in the surrounding fluid medium and visco-elastic/plastic behavior of the MEMS material. Most silicon MEMS operate at atmospheric pressure and the damping coefficient is dominated by the squeeze-film damping [68]. Reference [69] studied snap buckling of a shallow sinusoidal arch under a transient step mechanical pressure load and considered viscous damping. It has been reported in [69] that the critical pressure for the snap-through instability increased by about 3% due to a viscous damping coefficient of 1% of the critical damping and the large-amplitude motions after snap-through instability decay over time and the structure tends to the static snapped configuration.

4. Conclusions

Nonlinear governing equations (i.e. the continuum balance laws and Maxwell's equations) for an electrically actuated MEMS device have been summarized. These equations have been numerically solved to study finite transient deformations of a perfectly conductive body under the Coulomb pressure by coupling the FEM and the BEM: the former for the structural part of the problem and the latter for the electrical fields. The snap-through and the pull-in instabilities of micro-arches for different potential differences between the two electrodes have been studied. Depending upon how the electrical load is applied a micro-arch may experience either only the pull-in instability or the pull-in and the snap-through instabilities. It has also been found that the pull-in displacement is more for a micro-arch than that for a micro-beam of the same length, width, thickness and the initial gap as the micro-arch. The pull-in voltage obtained by analyzing the beam problem with the linear strain–displacement relation is nearly one-half of that for the same problem studied with the nonlinear strain–displacement relation.

The present work is of theoretical and practical significance and provides general theoretical results of the nonlinear behavior and instabilities of a micro-arch under transient nonlinear displacement-dependent electric loads. As a MEM electrode, micro-arches are advantageous over micro-beams because a micro-arch can have a larger operational range without the pull-in instability than a corresponding micro-beam. Moreover, by changing the rate of application of the potential difference between the two electrodes, the snap-through instability may be avoided. This provides another means to control the response of a MEMS device. Also, in a micro-arch under an electric load, the softening effect may be dominant before it experiences the snap-through instability but the strain-hardening effect may initially exceed the softening due to electric forces subsequent to the snap-through instability. This can be exploited in designing novel MEMS devices.

Acknowledgments

This work was partially supported by the Office of Naval Research grant N00014-06-1-0567 to Virginia Polytechnic

Institute and State University with Dr Y D S Rajapakse as the program manager. Partial support was also provided by Virginia Tech's Institute for Critical Technologies and Applied Sciences. Views expressed in the paper are those of the authors, and not of the funding agencies or of their institutions.

References

- [1] Rebeiz G M 2003 *RF MEMS Theory, Design, and Technology* (Hoboken, NJ: Wiley)
- [2] Roylance L M and Angell J B 1979 A batch-fabricated silicon accelerometer *IEEE Trans. Electron Devices* **26** 1911–7
- [3] Van Kessel P F, Hornbeck L J, Meier R E and Douglass M R 1998 A MEMS-based projection display *Proc. IEEE* **86** 1687–704
- [4] Bassous E, Taub H H and Kuhn L 1977 Ink jet printing nozzle arrays etched in silicon *Appl. Phys. Lett.* **31** 135–7
- [5] 2007 *Bio-MEMS: Technologies and Applications* (Boca Raton, FL: CRC/Taylor & Francis)
- [6] Taylor G 1968 The coalescence of closely spaced drops when they are at different electric potentials *Proc. R. Soc. A* **306** 423–34
- [7] Nathanson H C, Newell W E, Wickstrom R A and Davis J R Jr 1967 The resonant gate transistor *IEEE Trans. Electron Devices* **14** 117–33
- [8] Nguyen C T C, Katehi L P B and Rebeiz G M 1998 Micromachined devices for wireless communications *Proc. IEEE* **86** 1756–68
- [9] Hung E S and Senturia S D 1999 Extending the travel range of analog-tuned electrostatic actuators *Microelectromech. Syst. J.* **8** 497–505
- [10] Legtenberg R and Tilmans H A C 1994 Electrostatically driven vacuum-encapsulated polysilicon resonators: Part I. Design and fabrication *Sensors Actuators A* **45** 57–66
- [11] Krylov S, Seretensky S and Schreiber D 2007 Pull-in behavior of electrostatically actuated multistable microstructures *ASME 2007 International Design Engineering Technical Conference & Computers and Information in Engineering Conference (Las Vegas, NV, USA)*
- [12] Krylov S, Bojan R I, David S, Shimon S and Harold C 2008 The pull-in behavior of electrostatically actuated bistable microstructures *J. Micromech. Microeng.* **18** 055026
- [13] Vangbo M 1998 An analytical analysis of a compressed bistable buckled beam *Sensors Actuators A* **69** 212–6
- [14] Vangbo M and Bäccklund Y 1998 A lateral symmetrically bistable buckled beam *J. Micromech. Microeng.* **8** 29–32
- [15] Saif M T A 2000 On a tunable bistable MEMS-theory and experiment *Microelectromech. Syst. J.* **9** 157–70
- [16] Park S and Hah D 2008 Pre-shaped buckled-beam actuators: theory and experiments *Sensors Actuators A* **148** 186–92
- [17] Goll C, Bacher W, Buestgens B, Maas D, Menz W and Schomburg W K 1996 Microvalves with bistable buckled polymer diaphragms *J. Micromech. Microeng.* **6** 77–9
- [18] Kugel V D, Xu B, Zhang Q M and Cross L E 1998 Bimorph-based piezoelectric air acoustic transducer: model *Sensors Actuators A* **69** 234–42
- [19] Zhang Y, Wang Y, Li Z, Huang Y and Li D 2007 Snap-through and pull-in instabilities of an arch-shaped beam under an electrostatic loading *J. Microelectromech. Syst.* **16** 684–93
- [20] Krylov S, Seretensky S and Schreiber D 2008 Pull-in behavior and multistability of a curved microbeam actuated by a distributed electrostatic force *IEEE 21st Int. Conf. on Micro Electro Mechanical Systems, 2008 (MEMS 2008)* ed S Seretensky pp 499–502
- [21] Pippard A B 1990 The elastic arch and its modes of instability *Eur. J. Phys.* **11** 359–65
- [22] Patricio P, Adda-Bedia M and Ben Amar M 1998 An elastica problem: instabilities of an elastic arch *Physica D: Nonlinear Phenom.* **124** 285–95
- [23] Nayfeh A, Younis M and Abdel-Rahman E 2007 Dynamic pull-in phenomenon in MEMS resonators *Nonlinear Dyn.* **48** 153–63
- [24] Postma H W C, Kozinsky I, Husain A and Roukes M L 2005 Dynamic range of nanotube- and nanowire-based electromechanical systems *Appl. Phys. Lett.* **86** 223105
- [25] Flores G, Mercado G A and Pelesko J A 2003 Dynamics and touchdown in electrostatic MEMS *Proc. Int. Conf. on MEMS, NANO and Smart Systems, 2003* pp 182–7
- [26] Chu P B, Nelson P R, Tachiki M L and Pister K S J 1996 Dynamics of polysilicon parallel-plate electrostatic actuators *Sensors Actuators A* **52** 216–20
- [27] Ananthasuresh G K, Gupta R K and Senturia S D 1996 An approach to macromodeling of MEMS for nonlinear dynamic simulation *Proc. ASME Int. Conf. Mechanical Engineering Congress and Exposition (MEMS) (Atlanta, GA)* 401–7
- [28] Krylov S and Maimon R 2004 Pull-in dynamics of an elastic beam actuated by continuously distributed electrostatic force *J. Vib. Acoust.* **126** 332–42
- [29] Humphreys J S 1966 On dynamic snap buckling of shallow arches *AIAA J.* **4** 878–86
- [30] Budiansky B and Hutchinson J W 1964 Dynamic buckling of imperfection sensitive structure *TR 18, Contract 1866 (02), Div of Engineering and Applied Physics, Harvard Univ. (June 164) and AIAA J* **4** 525–30
- [31] Ganapathi M, Gupta S S and Patel B P 2003 Nonlinear axisymmetric dynamic buckling of laminated angle-ply composite spherical caps *Compos. Struct.* **59** 89–97
- [32] Gupta S S, Patel B P and Ganapathi M 2003 Nonlinear dynamic buckling of laminated angle-ply composite spherical caps *J. Struct. Eng. Mech.* **15** 463–76
- [33] Simites G J 1990 *Dynamic Stability of Suddenly Loaded Structures* (New York: Springer)
- [34] Batra R C, Porfiri M and Spinello D 2007 Review of modeling electrostatically actuated microelectromechanical systems *Smart Mater. Struct.* **16** R23–31
- [35] Tilmans H A and Legtenberg R 1994 Electrostatically driven vacuum-encapsulated polysilicon resonators: Part II. Theory and performance *Sensors Actuators A* **45** 67–84
- [36] Abdel-Rahman E M, Younis M I and Nayfeh A H 2002 Characterization of the mechanical behavior of an electrically actuated microbeam *J. Micromech. Microeng.* **12** 759–66
- [37] Younis M I, Abdel-Rahman E M and Nayfeh A 2003 A reduced-order model for electrically actuated microbeam-based MEMS *J. Microelectromech. Syst.* **12** 672–80
- [38] Liu Y, Liew K M, Hon Y C and Zhang X 2005 Numerical simulation and analysis of an electroactuated beam using a radial basis function *Smart Mater. Struct.* **14** 1163–71
- [39] Batra R C, Porfiri M and Spinello D 2006 Electromechanical model of electrically actuated narrow microbeams *J. Microelectromech. Syst.* **15** 1175–89
- [40] Batra R C, Porfiri M and Spinello D 2008 Vibrations of narrow microbeams predeformed by an electric field *J. Sound Vib.* **309** 600–12
- [41] Zhao X, Abdel-Rahman E M and Nayfeh A H 2004 A reduced-order model for electrically actuated microplates *J. Micromech. Microeng.* **14** 900–6
- [42] Nayfeh A and Younis M I 2004 Modeling and simulations of thermoelastic damping in microplates *J. Micromech. Microeng.* **14** 1711

- [43] Machauf A, Nemirovsky Y and Dinnar U 2005 A membrane micropump electrostatically actuated across the working fluid *J. Micromech. Microeng.* **15** 2309–16
- [44] Vogl G W and Nayfeh A H 2005 A reduced-order model for electrically actuated clamped circular plates *J. Micromech. Microeng.* **15** 684
- [45] Batra R C, Porfiri M and Spinello D 2008 Reduced-order models for microelectromechanical rectangular and circular plates incorporating the Casimir force *Int. J. Solids Struct.* **45** 3558–83
- [46] Batra R C, Porfiri M and Spinello D 2008 Vibrations and pull-in instabilities of microelectromechanical von Kármán elliptic plates incorporating the Casimir force *J. Sound Vib.* **315** 939–60
- [47] Ng T Y, Jiang T Y, Li H, Lam K Y and Reddy J N 2004 A coupled field study on the non-linear dynamic characteristics of an electrostatic micropump *J. Sound Vib.* **273** 989–1006
- [48] Mukherjee S, Bao Z, Roman M and Aubry N 2005 Nonlinear mechanics of MEMS plates with a total Lagrangian approach *Comput. Struct.* **83** 758–68
- [49] Telukunta S and Mukherjee S 2006 Fully Lagrangian modeling of MEMS with thin plates *J. Microelectromech. Syst.* **15** 795–810
- [50] Chao P C P, Chiu C W and Tsai C Y 2006 A novel method to predict the pull-in voltage in a closed form for micro-plates actuated by a distributed electrostatic force *J. Micromech. Microeng.* **16** 986–98
- [51] Hung E S and Senturia S D 1999 Generating efficient dynamical models for microelectromechanical systems from a few finite-element simulation runs *J. Microelectromech. Syst.* **8** 280–9
- [52] Pelesko J A 2001 Mathematical modeling of electrostatic MEMS with tailored dielectric properties *SIAM J. Appl. Math.* **62** 888–908
- [53] Batra R C, Porfiri M and Spinello D 2006 Analysis of electrostatic MEMS using meshless local Petrov–Galerkin (MLPG) method *Eng. Anal. Bound. Elem.* **30** 949–62
- [54] Pelesko J A, Bernstein D H and McCuan J 2003 Symmetry and symmetry breaking in electrostatically actuated MEMS *Nanotech* **2** 432–5
- [55] Nishiguchi I and Sasaki M 1994 A large deformation theory of solids subject to electromagnetic loads *IEEE Trans. Magn.* **30** 3272–5
- [56] Gilbert J R, Legtenberg R and Senturia S D 1995 3D coupled electro-mechanics for MEMS: applications of CoSolve-EM *Proc. IEEE Micro Electro Mechanical Systems (1995)* p 122
- [57] Shapoorabadi R J and Kirk A G 2004 Comparison of three finite element models for analysis of MEMS micromirrors *Proc. SPIE* **5577** 849–60
- [58] De S K and Aluru N R 2004 Full-Lagrangian schemes for dynamic analysis of electrostatic MEMS *J. Microelectromech. Syst.* **13** 737–58
- [59] Nelson D F 1979 *Electric, optic, and acoustic interactions in dielectrics* (New York: Wiley)
- [60] Batra R C, Porfiri M and Spinello D 2004 Treatment of material discontinuity in two meshless local Petrov–Galerkin (MLPG) formulations of axisymmetric transient heat conduction *Int. J. Numer. Methods Eng.* **61** 2461–79
- [61] Zienkiewicz O C, Taylor R L and Zhu J Z 2005 *Finite Element Method for Solid and Structural Mechanics* (Oxford: Elsevier Butterworth-Heinemann)
- [62] Pozrikidis C 2002 *A Practical Guide to Boundary Element Methods with the Software Library BEMLIB* (Boca Raton, FL: Chapman & Hall/CRC)
- [63] Radhakrishnan K and Hindmarsh A C 1993 *Description and Use of LSODE : the Livermore Solver for Ordinary Differential Equations* (Springfield, VA: National Aeronautics and Space Administration, Office of Management, Scientific and Technical Information Program)
- [64] Rochus V, Rixen D J and Golinval J-C 2006 Monolithic modelling of electro-mechanical coupling in micro-structures *Int. J. Numer. Methods Eng.* **65** 461–93
- [65] Mukhopadhyay S and Majumdar N 2006 Computation of 3D MEMS electrostatics using a nearly exact BEM solver *Eng. Anal. Bound. Elem.* **30** 687–96
- [66] Beer G, Smith I M and Duenser C 2008 *The Boundary Element Method with Programming: For Engineers and Scientists* (New York: Springer)
- [67] Batra R C, Porfiri M and Spinello D 2006 Capacitance estimate for electrostatically actuated narrow microbeams *Micro Nano Lett.* **1** 71–3
- [68] Andrews M, Harris I and Turner G 1993 A comparison of squeeze-film theory with measurements on a microstructure *Sensors Actuators A* **36** 79–87
- [69] Lock M H 1966 Snapping of a shallow sinusoidal arch under a step pressure load *AIAA J.* **4** 1249–56
- [70] Batra R C and Kim C H 1990 Adiabatic shear banding in elastic-viscoplastic nonpolar and dipolar materials *Int. J. Plast.* **6** 127–41
- [71] Batra R C and Liang X Q 1997 Finite dynamic deformations of smart structures *Comput. Mech.* **20** 427–38